

# Measured and projected beam backgrounds in the Belle II experiment at the SuperKEKB collider

A. Natochii<sup>a,\*</sup>, T. E. Browder<sup>a</sup>, L. Cao<sup>b</sup>, G. Cautero<sup>c,d</sup>, S. Dreyer<sup>b</sup>, A. Frey<sup>e</sup>, A. Gabrielli<sup>f,c</sup>, D. Giuressi<sup>c,d</sup>, T. Ishibashi<sup>g</sup>, Y. Jin<sup>c</sup>, K. Kojima<sup>h</sup>, T. Kraetzschmar<sup>i</sup>, L. Lanceri<sup>c</sup>, Z. Liptak<sup>j</sup>, D. Liventsev<sup>k,g</sup>, C. Marinasi<sup>l</sup>, L. Massaccesi<sup>m,n</sup>, K. Matsuoka<sup>g,o,h</sup>, F. Meier<sup>p</sup>, C. Miller<sup>q</sup>, H. Nakayama<sup>g,o</sup>, C. Niebuhr<sup>b</sup>, A. Novosel<sup>f</sup>, K. Parham<sup>p</sup>, I. Popov<sup>i</sup>, G. Rizzo<sup>m,n</sup>, J. M. Roney<sup>q</sup>, S. Y. Ryu<sup>s</sup>, L. Santelj<sup>t,r</sup>, S. Schneider<sup>p</sup>, J. Schueler<sup>a</sup>, B. Schwenker<sup>e</sup>, X. D. Shi<sup>g</sup>, F. Simon<sup>i</sup>, S. Stefkova<sup>b</sup>, M. Takahashi<sup>b</sup>, H. Tanigawa<sup>u</sup>, N. Taniguchi<sup>g</sup>, S. Terui<sup>g</sup>, S. E. Vahsen<sup>a</sup>, L. Vitale<sup>f,c</sup>, A. Vossen<sup>p</sup>, Z. Wang<sup>u</sup>, J. Wiechczynski<sup>v</sup>, H. Windel<sup>i,\*\*</sup>, K. Yoshihara<sup>h</sup>

<sup>a</sup>University of Hawaii, Honolulu, Hawaii 96822, USA

<sup>b</sup>Deutsches Elektronen-Synchrotron, 22607 Hamburg, Germany

<sup>c</sup>INFN Sezione di Trieste, I-34127 Trieste, Italy

<sup>d</sup>Elettra Sincrotrone Trieste SCpA, I-34149 Trieste, Italy

<sup>e</sup>II. Physikalisches Institut, Georg-August-Universität Göttingen, 37073 Göttingen, Germany

<sup>f</sup>Dipartimento di Fisica, Università di Trieste, I-34127 Trieste, Italy

<sup>g</sup>High Energy Accelerator Research Organization (KEK), Tsukuba 305-0801, Japan

<sup>h</sup>Graduate School of Science, Nagoya University, Nagoya 464-8602, Japan

<sup>i</sup>Max-Planck-Institut für Physik, 80805 München, Germany

<sup>j</sup>Hiroshima University, Higashi-Hiroshima, Hiroshima 739-8530, Japan

<sup>k</sup>Wayne State University, Detroit, Michigan 48202, U.S.A.

<sup>l</sup>Instituto de Fisica Corpuscular, Paterna 46980, Spain

<sup>m</sup>Dipartimento di Fisica, Università di Pisa, I-56127 Pisa, Italy

<sup>n</sup>INFN Sezione di Pisa, I-56127 Pisa, Italy

<sup>o</sup>The Graduate University for Advanced Studies (SOKENDAI), Hayama 240-0193, Japan

<sup>p</sup>Duke University, Durham, North Carolina 27708, U.S.A.

<sup>q</sup>University of Victoria, Victoria, British Columbia, V8W 3P6, Canada

<sup>r</sup>J. Stefan Institute, 1000 Ljubljana, Slovenia

<sup>s</sup>Research Center for Nuclear Physics, Osaka University, Osaka 567-0047, Japan

<sup>t</sup>Faculty of Mathematics and Physics, University of Ljubljana, 1000 Ljubljana, Slovenia

<sup>u</sup>Department of Physics, University of Tokyo, Tokyo 113-0033, Japan

<sup>v</sup>H. Niewodniczanski Institute of Nuclear Physics, Krakow 31-342, Poland

## Abstract

The Belle II experiment at the SuperKEKB electron-positron collider aims to collect an unprecedented data set of  $50 \text{ ab}^{-1}$  to study  $CP$ -violation in the  $B$ -meson system and to search for Physics beyond the Standard Model. SuperKEKB is already the world's highest-luminosity collider. In order to collect the planned data set within approximately one decade, the target is to reach a peak luminosity of  $6 \times 10^{35} \text{ cm}^{-2} \text{ s}^{-1}$  by further increasing the beam currents and reducing the beam size at the interaction point by squeezing the betatron function down to  $\beta_y^* = 0.3 \text{ mm}$ . To ensure detector longevity and maintain good reconstruction performance, beam backgrounds must remain well controlled. We report on current background rates in Belle II and compare these against simulation. We find that a number of recent refinements have significantly improved the background simulation accuracy. Finally, we estimate the safety margins going forward. We predict that backgrounds should remain high but acceptable until a luminosity of at least  $2.8 \times 10^{35} \text{ cm}^{-2} \text{ s}^{-1}$  is reached for  $\beta_y^* = 0.6 \text{ mm}$ . At this point, the most vulnerable Belle II detectors, the Time-of-Propagation (TOP) particle identification system and the Central Drift Chamber (CDC), have predicted background hit rates from single-beam and luminosity backgrounds that add up to approximately half of the maximum acceptable rates.

**Keywords:** Detector Background, Lepton Collider, Monte-Carlo Simulation

## 1. Introduction

The Belle II experiment [1, 2] studies  $CP$ -violation in the  $B$ -meson system and searches for Physics beyond the Standard Model, including evidence of dark sector particles, in decays of  $B$ -mesons,  $D$ -mesons and tau leptons [3]. The SuperKEKB collider [4] produces particles of interest by colliding electron and positron beams with asymmetric energies, mainly at the  $\Upsilon(4S)$  resonance. SuperKEKB is a major upgrade of KEKB [5, 6, 7]

\*Corresponding author

\*\*Now at Clinic for Cardiothoracic and Vascular Surgery, University Medical Center, 37075 Göttingen, Germany

Email addresses: natochii@hawaii.edu (A. Natochii), hiroyuki.nakayama@kek.jp (H. Nakayama), sevahsen@hawaii.edu (S. E. Vahsen)

and has been operational since 2016. The machine has already reached a world-record luminosity of  $4.65 \times 10^{34} \text{ cm}^{-2} \text{ s}^{-1}$  with a vertical betatron function of  $\beta_y^* = 1.0 \text{ mm}$  at the interaction point (IP), but the goal is to increase the luminosity by another order of magnitude in the coming decade, with a current target peak luminosity of  $6 \times 10^{35} \text{ cm}^{-2} \text{ s}^{-1}$  for  $\beta_y^* = 0.3 \text{ mm}$ . Luminosity increases by increasing beam currents and reducing the beam size at the IP, utilizing low-emittance colliding beams and the so-called nano-beam scheme [8].

Beam particles that deviate from the nominal orbit are eventually lost by hitting the beam pipe's inner wall or other machine apparatus. If the loss position is close to the Belle II, generated shower particles might reach the detector and increase its dose rate and hit rate. This increase is referred to as “beam (induced) background” and is one of the most difficult challenges at SuperKEKB. In the SuperKEKB and Belle II designs, it was estimated that several Belle II sub-detectors would be subject to close-to-tolerable backgrounds at the target peak luminosity [9, 10]. The most vulnerable sub-detectors are the Time-of-Propagation (TOP) particle identification system and the Central Drift Chamber (CDC). In the TOP, higher hit rates increase the accumulated output charge in the micro-channel-plate photo-multiplier tubes (MCP-PMTs) used to read out Cherenkov photons propagated in quartz bars, which can degrade the quantum efficiency of the PMTs. One key issue in the CDC is that pattern recognition of charged tracks becomes increasingly difficult as the wire-hit rate increases.

Given the importance of beam background mitigation to the experiment's success, we have studied such backgrounds extensively in the early stages of SuperKEKB running. The Belle II/SuperKEKB project has three major commissioning phases:

- *Phase 1* was carried out in Spring 2016. No beam collisions occurred, as SuperKEKB was running without the final focusing system. Belle II had not yet been installed at the IP. Instead, a system of dedicated beam background detectors, collectively known as BEAST II, was placed around the IP. We found that the background level around the IP was safe for Belle II to be installed. Results of the Phase 1 measurements and simulation are reported in Ref. [10].
- *Phase 2* began in March 2018 and concluded in July 2018. The machine group demonstrated first the  $e^+e^-$  collisions with Belle II (except for the vertex detector) now installed at the IP. This commissioning phase confirmed that proceeding and installing the sensitive vertex detector was safe. Details and results of the Phase 2 beam background study can be found in Ref. [11].
- *Phase 3*, which started in March 2019, is dedicated to physics data taking with a fully instrumented Belle II detector and to increasing the instantaneous luminosity above  $1 \times 10^{35} \text{ cm}^{-2} \text{ s}^{-1}$ . We aim to accumulate  $50 \text{ ab}^{-1}$  of data by the 2030s, anticipating 7–8 months of operation per year, and assuming 70% of that operation time is spent on physics runs [12].

In the rest of Section 1, we describe the SuperKEKB collider and the Belle II detector and provide an overview of the main beam-induced background sources, background countermeasures, and relevant beam instrumentation. Section 2 reports on the current (early Phase 3) background levels and safety margins of the Belle II sub-detectors. In Section 3, we describe the beam background Monte-Carlo (MC) simulation methodology. In Section 4, we explain the methodology of background measurements and modeling. Section 5 reports on the measured background composition in Belle II. In Section 5 we also apply correction factors of each simulated background process in each sub-detector to enforce a full agreement with measurements. This detailed model is required to reliably extrapolate the current backgrounds to different beam conditions. Section 6 describes an extrapolation of backgrounds towards higher luminosity and provides expected detector safety factors<sup>1</sup>. Finally, in Section 7, we summarize and discuss our findings and their implications.

### 1.1. SuperKEKB and Belle II

Here, we briefly review the collider and detector sub-systems involved in the beam-induced background analysis. Further details can be found in Refs. [1, 2, 4].

*SuperKEKB*, illustrated in Fig. 1, is an upgrade of the KEKB accelerator. It is a 3 km-circumference asymmetric-energy electron-positron collider with a center-of-mass (CM) energy of  $\sqrt{s} = 10.58 \text{ GeV}$  which corresponds to the mass of the  $\Upsilon(4S)$  resonance. At the IP, 7 GeV electrons stored in the high-energy ring (HER) collide with 4 GeV positrons accumulated in the low-energy ring (LER). To reach collision luminosity of the order of  $1 \times 10^{35} \text{ cm}^{-2} \text{ s}^{-1}$ , SuperKEKB utilizes the so-called nano-beam scheme, where the vertical and horizontal beam sizes at the IP are squeezed down to  $\sim 50 \text{ nm}$  and  $\sim 10 \mu\text{m}$ , respectively, with a horizontal crossing angle of 83 mrad to avoid the hour-glass effect. The relatively large crossing angle also allows i) a new final focusing system with superconducting quadrupole magnets (QCS) to reside closer to the IP, ii) separate beamlines for the HER and LER, and iii) a design that avoids combined-function IP magnets. To eliminate luminosity degradation caused by beam-beam resonances, dedicated sextupole magnets are used for the Crab-Waist collision scheme implementation [13], which aligns the vertical waistline of one beam along the trajectory of the other beam at the IP.

The upgrade from KEKB to SuperKEKB included the following major items. We note that the list is not exhaustive.

- Short LER dipole magnets were replaced with longer ones.
- The interaction region (IR),  $\pm 4 \text{ m}$  around the IP, was re-designed. This region hosts the Belle II detector, the final focusing system and the IR beam pipe assembly.
- Beam pipes with a titanium nitride (TiN) coating and antechambers were installed in the LER to reduce the power

<sup>1</sup>The safety factor is defined as a ratio between the detector limit and predicted background rate. It shows how much the background level can increase before reaching the detector limit.

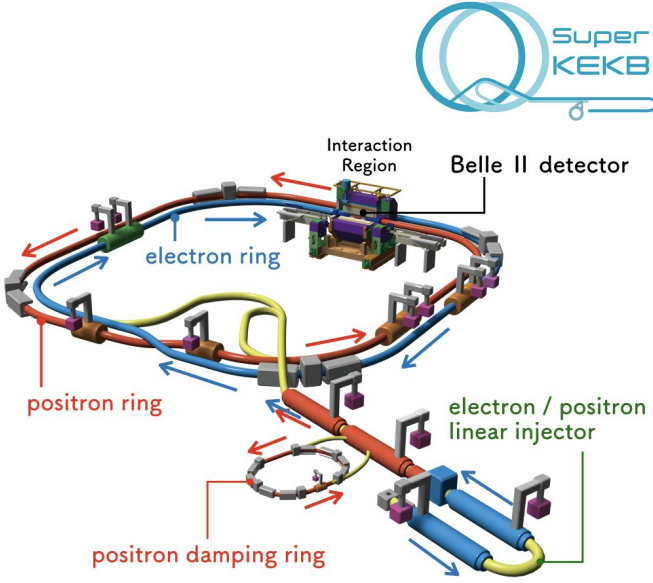


Figure 1: Schematic drawing of the SuperKEKB collider.

density of the synchrotron radiation (SR) and to suppress electron-cloud formation.

- A damping ring (DR) was constructed to reduce the injected positron beam emittance.
- The radio-frequency (RF) system was modified to enable higher beam currents.
- The collimation system was upgraded, see Section 1.3.

There are two major upgrades of SuperKEKB planned in the next decade, during Long Shutdown 1 (LS1), which began in July 2022, and during Long Shutdown 2 (LS2), expected to begin around 2027. Possible future upgrades of the detector are strongly linked to upgrades of the machine. The most crucial upgrades under consideration are discussed in Ref. [14]. The *Belle II* detector, shown in Fig. 2, is a general-purpose particle spectrometer optimized for precise measurements of  $B$ -meson pairs via their decay products. The detector must maintain Belle's level of performance [15, 16], despite a reduced center of mass boost, and while operating in a much higher-background environment, which tends to reduce detector performance and longevity. Belle II replaced a number of Belle sub-systems to satisfy this requirement and to have better vertexing and particle identification performance than Belle. Belle II consists of several nested sub-detectors around the 1-cm radius beryllium beam pipe surrounding the IP. The Belle II sub-detector closest to the IP is the two-layer pixel detector (PXD). All 16 modules in the first PXD layer (L1), but only 4 out of the 24 modules in the second PXD layer (L2) have been installed to date. During LS1, we plan to install a new, fully assembled two-layer PXD, which will increase the detector's performance and tolerance of hit occupancy due to back-

grounds [17]. The PXD is surrounded by four layers (L3-6) of the double-sided silicon strip vertex detector (SVD). Both PXD and SVD are surrounded by the CDC, which is filled with a  $\text{He}(50\%) + \text{C}_2\text{H}_6(50\%)$  gas mixture. The CDC consists of 56 layers with 14336 sense wires of either axial or stereo orientation for precise measurements of charged particle trajectories. The charged-particle identification system is based on two sub-detectors: the barrel's TOP detector and the Aerogel Ring Imaging Cherenkov counter (ARICH) in the forward endcap region. The TOP is composed of 2-cm-thick quartz bars viewed by conventional and atomic layer deposition (ALD) types of MCP-PMTs, which are arranged into 16 readout slots. The ARICH consists of 4-cm-thick focusing aerogel radiators and 420 Hybrid Avalanche Photo Detectors (HAPDs), each having 144 readout channels. For precise energy and timing measurements of particles, an electromagnetic calorimeter (ECL) is installed in the barrel and both endcaps. It is composed of 8736 CsI(Tl) crystals and is located inside a superconducting solenoid that provides a 1.5 T magnetic field. Outside the magnet coil, a  $K_L^0$  and muon detector (KLM) is installed. The KLM has 12 and 14 scintillator strip layers read out by silicon photomultipliers in the forward (FWD) and backward (BWD) endcaps, respectively. The two innermost KLM barrel layers also utilize scintillators, while the remaining 13 barrel layers consist of glass-electrode resistive plate chambers (RPCs). A comprehensive overview of Belle II upgrades planned for LS1 and LS2 can be found in Ref. [17].

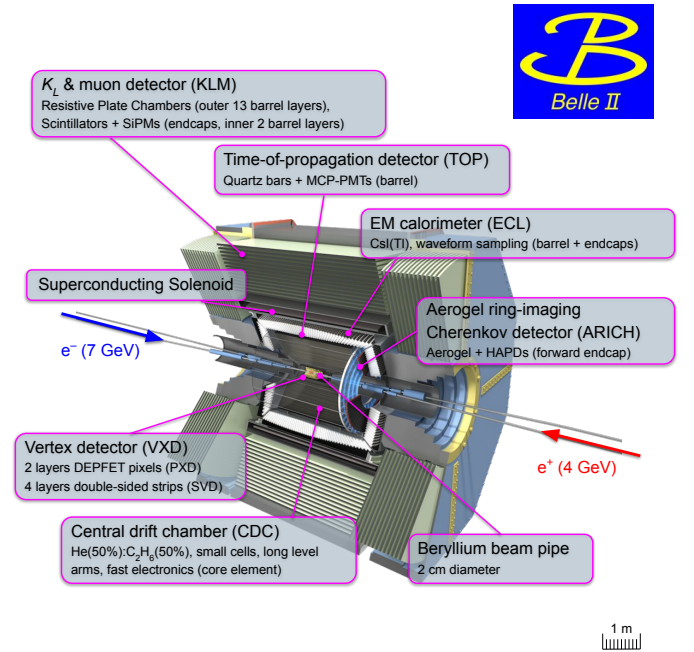


Figure 2: Overview of the Belle II detector.

## 1.2. Background types

Belle II hits generated by background shower particles deteriorate the detector's physics performance. The radiation dose

and neutron fluence from the background showers can also damage sensor components in the detector, such as silicon devices. Below we review the leading background components that are relevant at SuperKEKB.

*Touschek background.* Touschek scattering [18], one of the leading background sources at SuperKEKB, refers to Coulomb scattering between two particles in the same beam bunch. Such scattering causes the energies of the two scattered particles to deviate from the nominal beam energy, with one particle gaining, and the other losing, energy. The Touschek scattering rate is proportional to the beam current squared and inversely proportional to the number of bunches in the ring and the beam size. Due to the nano-beam scheme used at SuperKEKB, the beam size is much smaller than at KEKB, and consequently, the ring-integrated beam loss rate due to Touschek scattering is expected to be much higher. However, the Touschek loss rate inside Belle II has been significantly suppressed by installing horizontal collimators near the IR.

*Beam-gas background.* Beam-gas scattering by residual gas atoms in the beam pipe is another major background source at SuperKEKB. Beam-gas Coulomb scattering changes the direction of scattered beam particles, while beam-gas bremsstrahlung scattering reduces their energy. The beam-gas scattering rate is proportional to the residual gas pressure and to the beam current. The beam-gas Coulomb loss rate inside Belle II is expected to be quite high due to the small diameter of the IP beam pipe and the extremely large vertical betatron function of the QCS. The loss rate in the detector has been greatly reduced by installing vertical collimators. However, the aperture of those collimators must be narrowed by moving their jaws towards the beam core, which can induce beam instabilities at high beam currents [19].

*Luminosity background.* Luminosity background is caused by beam collisions at the IP. It is proportional to luminosity and expected to dominate at the target luminosity of SuperKEKB, which is about 30 times higher than the record of KEKB.

One important luminosity background is from radiative Bhabha scattering ( $e^+e^- \rightarrow e^+e^-\gamma$ ), where beam particles lose energy by emitting photons and therefore deviate from the nominal orbit. At KEKB, since a shared final focusing magnet scheme was employed, the outgoing beam orbits were off-center in the quadrupole magnets. Therefore, off-energy beam particles were strongly over-bent and easily lost inside the detector. Unlike KEKB, the final focusing magnets at SuperKEKB are separate for each ring, which relaxes the loss rate inside the detector. However, a small fraction of beam particles with large energy losses can still be lost inside the detector due to i) the strong magnetic field of the final focusing magnets, ii) intrinsic beam angular divergence at the IP, iii) angular diffusion by the radiative Bhabha process, iv) the kick from the detector solenoid field, and v) the leakage field from the other ring's quadrupole magnets, especially for electrons as discussed in Ref. [20]. At high luminosity, radiative Bhabha beam losses inside the detector dominate over other Belle II backgrounds.

Radiative Bhabha scattering can also give rise to neutron backgrounds incident upon Belle II from the accelerator tunnel via the following mechanism: photons emitted in the radiative Bhabha process at the IP propagate along the beam axis and escape Belle II. Such photons then hit accelerator magnets located 10–20 m downstream of the IP. Then, neutrons copiously produced via the giant photo-nuclear resonance [21] scatter back towards the Belle II detector. This background increases the hit occupancy in the outer layers of the KLM. A dedicated study of this background component is described in Ref. [22].

In the two-photon process,  $e^+e^- \rightarrow e^+e^-e^+e^-$ , beam particles lose energy by emitting low-momentum electron-positron pairs, and become a source of Belle II background as described for the radiative Bhabha process. In addition, the emitted electron and positron curl in the Belle II solenoid field. They can leave multiple hits in the inner Belle II detectors if they have high enough transverse momentum.

*Synchrotron radiation background.* SR emitted from the beams is another source of background in the inner Belle II detectors. Since the power of SR is proportional to the beam energy squared and the magnetic field strength squared, the HER electron beam is the main source of SR background. SR photons leave PXD and SVD hits with energy ranging from a few keV to several tens of keV. We pay special attention to this background because the inner layers of the SVD were severely damaged by HER SR in the early stages of the Belle experiment.

*Injection background.* Since the beam lifetime of SuperKEKB is much shorter than an hour, top-up injections via a betatron injection scheme [4] are performed during physics data taking. When the total beam current is below a set threshold ( $\sim 99\%$  of the nominal beam current), charge is injected into buckets with low bunch-current, at a certain repetition rate (1–25 Hz). Newly injected bunches are perturbed and oscillate in the horizontal plane around the main stored beam. This causes increased background rates in Belle II for a few milliseconds (ms) after injection each time when the newly injected bunch passes the IP. In order to avoid saturation of the readout, special trigger vetoes are applied, which lead to dead time in the data acquisition and, consequently, a reduction in recorded luminosity. A comprehensive description of the Belle II trigger system is given in Ref. [3].

The amount and time structure of the injection background observed in Belle II is shared online with the SuperKEKB operators and can be used to optimize the injection settings to keep backgrounds low. One of the most important and difficult tasks for SuperKEKB is maintaining stable injection background conditions for an extended period.

*Large beam loss accidents.* The accidental firing of one of the injection kicker magnets may perturb the stored beam during its 2- $\mu$ s-long waveform towards a horizontal collimator, causing severe jaw damage.

Furthermore, for unknown reasons, the stored beam sometimes becomes unstable to the point of causing catastrophic or so-called *sudden beam losses*. These losses have already caused



several quenches of QCS magnets, damaged sensitive components of Belle II, and significantly slowed down the planned luminosity increase. In other cases, the jaws of collimators were severely damaged, and beam operation was stopped for about a week to replace the jaws. Such events frequently occur when the beam current increases above 0.5 A. A possible cause of these events is dust trapped in the beam pipe, but this is not yet fully understood. We are conducting detailed beam abort analysis using the timing information from the beam loss monitors installed around the ring. Such analysis may help us to identify the location where the initial beam loss occurred.

### 1.3. Background mitigation

Here, we briefly review the crucial countermeasures against major, known background sources.

**Collimators.** Movable beam collimators are installed around SuperKEKB rings to stop beam particles with large transverse deviation from the nominal beam orbit before they reach the IR and lead to background hits in Belle II, see Fig. 3. Moreover, the collimators help protect Belle II and the QCS magnets against large, unexpected beam losses, including those from accidental injection kicker firing.

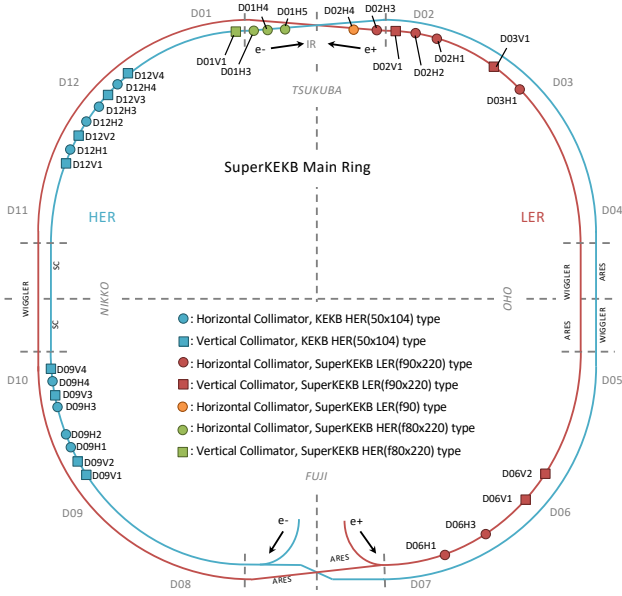


Figure 3: Map of the SuperKEKB collimators used in 2021 and 2022. The letters V and H in the collimator names indicate vertical and horizontal movable jaws, respectively. There are twelve sections in each ring named D01 through D12.

There are currently 11 collimators in the LER and 20 in the HER, see Fig. 3. There are two main types of collimators with different geometries: *KEKB-type* collimators are asymmetric and have only one jaw, while *SuperKEKB-type* collimators are symmetric with jaws on both sides. More details about the collimators can be found in Refs. [23, 24].

Horizontal collimators effectively stop Touschek scattered particles, while vertical collimators are mainly used to stop beam-gas Coulomb scattered particles. The vertical collimators must be closed to very small apertures of the order of 1 mm, and therefore require a precise position control system. The small apertures can induce Transverse Mode Coupling Instabilities (TMCI) of the stored beam. They contribute to the overall machine impedance, resulting in an upper limit on the bunch current for stable operation [25],

$$I_{\text{thresh.}} = \frac{4\pi f_s E/e}{\sum_j \beta_j k_j}, \quad (1)$$

where  $I_{\text{thresh.}}$  is the the bunch current threshold,  $f_s$  is equal to 2.13 kHz and 2.80 kHz for the LER and HER synchrotron frequency, respectively,  $E$  is the beam energy,  $e$  is the unit charge, and  $\beta_j$  and  $k_j$  are the beta function and kick factor [23] of the  $j$ -th collimator, respectively. In contrast, wide-open collimators increase beam losses in the IR, while too-narrow collimators reduce beam lifetime and injection efficiency. Therefore, each collimator should be set at the aperture that optimally balances backgrounds, lifetimes, injection performance and instabilities [19].

In our previous work on beam backgrounds [23], the simulation of the SuperKEKB collimation system was substantially improved, and it is now deemed reliable.

**Detector shielding.** While collimators successfully reduce single-beam losses inside Belle II, some fraction of stray beam particles still escape the collimators and are lost inside the detector. To protect the inner detectors from single-beam and luminosity background showers, tungsten shields are installed just outside the IP beam pipe and inside the vertex detector, but outside of the detector acceptance for physics signals. In addition, thick tungsten shields are also installed around the QCS, where the beam loss rate is estimated to be the highest due to a large betatron function.

**IP beam pipe.** The IP beam pipe of SuperKEKB is carefully designed to reduce the SR background [1, 26]. SR from upstream of the IP is stopped by a tapered collimation part of the incoming pipe so that SR will not hit the central beryllium part of the IP beam pipe. Reflected SR will also not reach the central IP beam pipe, thanks to a ridge structure on the tapered surface of the incoming beam pipe. In addition, the effect of back-scattered SR is significantly reduced in SuperKEKB compared to KEKB. Because there is a separate QCS magnet for each ring, the outgoing beam orbit is almost straight and does not produce an SR fan.

### 1.4. Beam instrumentation relevant to background measurements

This section lists the essential instrumentation (other than Belle II) utilized to monitor beam parameters, the vacuum pressure in the beam pipe, and background levels at SuperKEKB.

*Beam diagnostics.* In SuperKEKB, transverse beam sizes are measured by X-ray beam profile monitors (XRMs) and visible synchrotron radiation monitors (SRMs). For the analyses reported here, XRM data are used. The X-ray imaging system uses Cerium-doped yttrium-aluminum-garnet (YAG:Ce) scintillators combined with CMOS cameras [27]. A coded aperture imaging technique provides turn-by-turn vertical and horizontal beam size measurements with a spatial resolution of the order of 1  $\mu\text{m}$  and 10  $\mu\text{m}$ , respectively [28]. The bunch length is measured using a streak camera installed in each ring. Dedicated machine time is required to scan bunch lengthening from low ( $\sim 0$  mA/bunch) to high ( $\sim 1.4$  mA/bunch) bunch currents and to separate the lengthening due to single-beam effects, such as the longitudinal wakefield potential, from other influences, possibly from beam-beam interactions. Therefore, bunch length data are usually measured only once a year, to minimize interruptions of Belle II data taking. Instantaneous and integrated luminosity measurements are provided by the Luminosity Online Monitor (LOM), which is based on the rate of Bhabha scattering events measured by the ECL [29]. At a counting rate of about 1 Hz, the system’s statistic accuracy is 5% at a luminosity of  $1 \times 10^{34} \text{ cm}^{-2} \text{ s}^{-1}$  and the overall systematic uncertainty is estimated to be at the level of 1.7%.

*Vacuum system.* The vacuum system of the collider is designed to effectively mitigate i) higher order mode (HOM) power losses, ii) heat and gas loads due to the large SR power and photon density, and iii) the electron cloud and fast ion effects in the LER and HER, respectively. A distributed pumping system based on multilayer non-evaporable getter (NEG) strips [30] is used to keep the vacuum pressure at the level of 100 nPa, which is required to achieve hours-long beam-gas lifetime. To measure the residual gas pressure in the collider beam pipe, about 300 cold cathode gauges (CCGs) are installed around each ring in roughly 10 m intervals. These CCGs provide ultra-high vacuum pressure measurements above 10 nPa. A dedicated vacuum pressure simulation shows that in the absence of circulating beams, the so-called *base* gas pressure is almost the same at the center of the beam pipe as in the vicinity of the CCG. However, due to the finite conductance of the vacuum system, composed of the beam pipe, CCG, and vacuum pump, the *dynamic* part of the pressure, which depends on the beam current and gas molecule desorption rate from the inner beam pipe walls, is approximately three times higher at the beam axis than at the CCGs; this factor was estimated from a simulation taking into account the conductance of the RF-shield screen between the beam channel and the pumping port and that of the pumping port itself [31]. This factor of three, which is the same for both rings, is used in the beam-gas background study discussed later in the text.

SuperKEKB is instrumented with two residual gas analyzers (RGAs) in the D02 and D06 ring sections, see Fig. 3, to measure the molecular composition of residual gases in the beam pipe. These devices are mass spectrometers measuring mass-to-charge ratios of gas ion fragments. Due to the small number of RGAs, reliable information regarding the gas composition distribution around the collider is currently unavailable. There-

fore, in simulation, an effective atomic number of  $Z_{\text{eff}} = 7$ , mostly due to CO molecules, is assumed for the residual gas in the beam pipe [32].

*Background monitors.* Several dedicated detector systems are used to monitor backgrounds in the SuperKEKB IR and tunnel, and to ensure safe machine and detector operation.

- Diamond sensor-based detectors (Diamonds) [33] are used for radiation dose rate measurements in the IR, as shown in Fig. 4, where rectangles highlighted in blue and green indicate detectors used for dose rate monitoring at a 10 Hz readout rate and fast beam abort monitoring at 400 kHz, respectively.
- The sCintillation Light And Waveform Sensors (CLAWS) detector system [34] is based on plastic scintillators and silicon photomultipliers. It monitors beam-induced backgrounds synchronized with the SuperKEKB injection. There are in total 32 CLAWS modules with 16 on the forward and 16 on the backward side of the IR around the final focusing magnets. The modules are located in four different longitudinal positions along the beam direction (approximately 1, 2, 3, and 4 m from the IP) and four different azimuth angles ( $0^\circ$ ,  $90^\circ$ ,  $180^\circ$  and  $270^\circ$ ) on each of the magnets.
- The BEAST TPC system uses six compact, high-resolution gaseous detectors [35] to provide directional and spectral measurements of the fast neutron flux [22]. Currently, the detectors are located in the accelerator tunnel near Belle II.
- Four  $^3\text{He}$  tube detectors [36], installed around Belle II, count thermal neutrons with kinetic energy below about 0.025 eV through the following process:  

$$^3_2\text{He} + ^1_0\text{n} \rightarrow ^3_1\text{H} + ^1_1\text{H} + 764 \text{ keV}$$
- PIN photo-diodes [37] installed next to each collimator are used for fast beam loss monitoring around the movable jaws.
- 5-m-long ion chambers [37] are mounted in cable racks on the outer wall along the accelerator tunnel. These air-filled gaseous detectors are used to measure beam losses.
- New loss monitors, based on CsI-crystals with photomultiplier tubes (PMTs) and electron-multiplier tubes (EMTs), were recently installed near SuperKEKB collimators. These new systems with good time synchronization capabilities are now used to pin down the location of sudden beam losses around the rings.

*Beam abort system.* A dedicated fast beam abort system is used to dump unstable beams in order to avoid severe machine or detector damage. During commissioning Phases 1 and 2, the abort system included Diamonds (green rectangles, see Fig. 4), PIN photo-diodes and ionization chambers. In Phase 3, the system was augmented by including the four forward and four backward CLAWS detectors closest to the IP. These detectors can

trigger a beam abort  $\sim 10 \mu\text{s}$  earlier than Diamonds, on average.

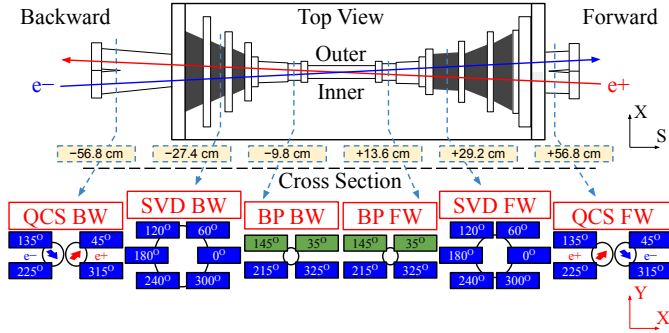


Figure 4: Locations of diamond detectors in the IR. The dashed rectangles show the distance from the IP along the beam axis for each group of detectors. Azimuth angles of the detectors are indicated in rectangles. See text for further details.

## 2. Current background levels and margin

Here, we specify the main background vulnerabilities of each sub-detector. We also report on i) the current background rates seen during Belle II operation in 2021, ii) the margin with respect to maximum acceptable rates, and iii) the recently observed detector performance degradation in 2022.

### 2.1. PXD

PXD is the inner-most detector, and its expected dominant background originates from the irreducible two-photon process where the low-momentum electron-positron pair spirals through the detector. Injection background and sudden beam losses are also of particular concern. The passing particles can deposit significant doses shortening the detector's lifetime and damage the detector by creating dead pixels or inefficient regions. As the closest detector to the IP, the PXD is also uniquely sensitive to the back-scatter of low-energy SR photons.

First, there is a limit on acceptable PXD occupancy due to bandwidth limitations. Assuming 30 kHz trigger rate operation, some data loss will start to occur once the mean of the inner PXD layer occupancy exceeds 3%. At 3% occupancy, the offline performance will also degrade significantly because of cluster merging and an increased probability of associating wrong hits to tracks. Noticeable degradation, however, starts below this value.

The PXD's second limit is associated with detector degradation due to radiation damage. A dose rate of 2 Mrad/smy<sup>2</sup> for a 10-year-long operation of the device is deemed safe given the results from a dedicated X-ray irradiation campaign [38]. Type inversion is not expected to occur before reaching a 1-MeV neutron equivalent fluence<sup>3</sup> of  $1 \times 10^{14} \text{ n}_{\text{eq}}/\text{cm}^2$ .

<sup>2</sup>The unit smy stands for a Snowmass year ( $1 \times 10^7 \text{ s}$ ), which is the typical operation time of an accelerator facility.

<sup>3</sup>The 1-MeV neutron equivalent fluence is the fluence of 1 MeV neutrons producing the same damage in a detector material as produced by an arbitrary particle fluence with a specific energy distribution [39, 40].

The current average PXD occupancy is below 0.3%, suggesting PXD background levels are under control. At least once a year, however, significant beam losses have occurred, where 4–5% of the so-called PXD switcher<sup>4</sup> channels were damaged. This makes the planned replacement of the current PXD with a new two-layer PXD during LS1 particularly valuable.

Extrapolating current background levels to the predicted beam parameters before LS2 at the luminosity of  $2.8 \times 10^{35} \text{ cm}^{-2} \text{ s}^{-1}$ , the PXD should be able to withstand the backgrounds and operate with a predicted average occupancy below 0.5%, assuming the collimators can be operated close to ideal settings, and the total PXD background, including storage and injection components, stays below the detector limit.

### 2.2. SVD

In the SVD, the beam background increases the hit occupancy and causes radiation damage in the sensors. The increased hit occupancy, in turn, degrades the SVD tracking performance and increases data rates in the data acquisition system (DAQ). Radiation damage can affect the sensor leakage current, strip noise, and the full depletion voltage of sensors. It is important to estimate the expected SVD performance degradation over the entire lifetime of the experiment, given the expected background levels.

Radiation effects, respectively, from surface and bulk damage, are parameterized in terms of total ionizing dose released in the sensor (TID) and with non-ionizing energy loss (NIEL), expressed in a 1-MeV neutron equivalent fluence. Effects due to surface damage saturate after a relatively low integrated dose, about 100 krad, while bulk effects are expected to dominate the SVD radiation damage in the long term.

The most restrictive limit on the SVD beam background levels is due to the degradation of the tracking performance, which limits the hit occupancy of the SVD inner-most layer (L3) to about 5%, with a rejection of background hits based on the hit-time, that can be further refined. As for the integrated radiation damage, a deterioration of the SVD performance is expected after about 6 Mrad, corresponding to about  $1.4 \times 10^{13} \text{ n}_{\text{eq}}/\text{cm}^2$  of 1-MeV neutron equivalent fluence, due to a sizable reduction in the Signal-to-Noise. After this level of irradiation, the increase in the sensor current, dominated by bulk damage, will produce noise from leakage current comparable to the one from the sensor capacitance, now dominant, thus increasing the noise by about  $\sqrt{2}$ . As for changes in the effective doping concentration and depletion voltage, no significant performance degradation is expected even after bulk type inversion and up to about  $2.5 \times 10^{13} \text{ n}_{\text{eq}}/\text{cm}^2$ . This limit is based on the results of sensors used in the BaBar experiment, similar to the SVD ones, that were confirmed to be fully functional after irradiation up to this level [41].

Electrons and positrons are the dominant sources of beam background in the SVD, contributing to the hit occupancy and

<sup>4</sup>The PXD switchers are the readout ASICs that switch on a pixel row to send the currents to the Drain Current Digitizers, which digitize the MOSFET currents from a row of pixels [1].

to radiation damage. Neutrons and hadrons are the most effective for bulk damage, but it should be noted that electrons and positrons in the MeV-GeV energy range also contribute to bulk damage, although with a reduced effective cross-section for NIEL, properly accounted for in the conversion from particle fluence to 1-MeV neutron equivalent fluence. Electrons and positrons are either produced at the IP by the beam collisions or created off-IP by the scattering of the beam loss products in the accelerator components or the detector material and finally hitting the SVD. Neutrons are created off-IP and, although less abundant in the SVD, contribute via NIEL to the bulk radiation damage.

During operation in 2021, the hit occupancy averaged over the L3 sensors was 0.5% at maximum, well below the occupancy limit of about 5%. In the three-year operation of the SVD, from 2019 to 2021, the first effects of radiation damage have been measured, consistent with expectation, and with no degradation of the SVD performance [42].

The SVD is not always energized unlike the diamond sensors. Therefore, the integrated dose in the SVD is estimated from the dose measured by the diamond sensors on the beam pipe, and the measured correlation between the SVD occupancy and the diamond dose [42, 43]. The estimated integrated dose in the SVD L3 was about 50 krad up to December 2021. The 1-MeV neutron equivalent fluence was evaluated to be about  $1.2 \times 10^{11} \text{ n}_{\text{eq}}/\text{cm}^2$ , using a conversion factor from the integrated dose to the neutron equivalent fluence estimated by simulation.

Given the SVD limits of about 5% in L3 occupancy and about 6 Mrad integrated dose, the SVD will be able to withstand, with a good safety margin, the background levels predicted before LS2 at the luminosity of  $2.8 \times 10^{35} \text{ cm}^{-2} \text{ s}^{-1}$ , corresponding to about 1% occupancy in L3 and about 70 krad/smy.

### 2.3. CDC

As the main tracking detector of Belle II, a well-performing CDC is not only essential for tracking and the measurement of particle momenta but also for trigger information and particle identification via the measurement of specific ionisation in the chamber gas ( $dE/dx$ ). Extra background hits caused in particular by LER Touschek and beam-gas scattering processes as well as by the injection background progressively degrade the CDC performance as the rate of background hits increases. The additional background hits can contaminate the physical signal of charged tracks, creating spurious tracks and smearing the kinematic variables of the reconstructed charged track. Higher background levels also increase the overall current in the chamber, increasing the risk of more rapid chamber ageing due to an accelerated buildup of deposits on the wires. Finally, an increasing rate of single-event upsets (SEUs) in the front-end electronics of the CDC, caused by background neutrons with low kinetic energy, is another concern for the CDC operation [44]. SEUs or other kinds of CDC soft errors may stop the DAQ of Belle II and decrease the data-taking efficiency. A planned upgrade of readout electronics during LS2 is expected to suppress the soft error rates.

The effect of background hits on the performance of the tracking algorithm has been studied with Monte-Carlo simu-

lations [45]. To avoid degradation of the tracking performance, based on simulation at the luminosity of  $1.2 \times 10^{35} \text{ cm}^{-2} \text{ s}^{-1}$ , a background hit rate of 150 kHz/wire is acceptable, where the SVD stand-alone tracking retains high efficiency and CDC hits can be added to the SVD seed tracks. The CDC hit rates in 2021 for all layers were in the range from 20 kHz/wire to 50 kHz/wire, except for the first, inner-most layer with a hit rate of up to 130 kHz/wire. The extrapolation of the background before LS2 at the luminosity of  $2.8 \times 10^{35} \text{ cm}^{-2} \text{ s}^{-1}$  shows the CDC can run safely at beam currents up to  $\sqrt{I_{\text{LER}} I_{\text{HER}}} \sim 2.0 \text{ A}$ . The hit rates, except for the first layer, will reach 50–130 kHz/wire depending on the radial position of the layers, which is below the detector's limit. However, this simulation does not include the effect of the injection background during the trigger veto period, which leads to a strongly time-dependent overall chamber current.

### 2.4. ARICH

For the ARICH detector, there are three main adverse effects resulting from the beam-induced background. The first effect is neutron-induced silicon bulk damage in the avalanche-photo-diode chips (APDs) of the photon detectors (HAPDs), and the second is the Cherenkov photon background, mostly emitted by low-energy charged particles either in the aerogel or in the quartz window of the photon detectors. As a result of the first effect, the APD leakage current is steadily increasing with accumulated neutron fluence, eventually leading to a reduced Signal-to-Noise ratio and consequently either to the loss of photon detection efficiency or increased background hit rate. The increased background hit rate, resulting either from the APD noise or from the background Cherenkov photons, negatively impacts the ARICH particle identification performance. In neutron irradiation tests of HAPDs carried out prior to the ARICH construction, the leakage current remained tolerable ( $< 30 \mu\text{A}/\text{APD}$ ) at least up to a fluence of  $\sim 1 \times 10^{12} \text{ n}_{\text{eq}}/\text{cm}^2$ , which we consider as a conservative limit. The tolerable background photon hit rate was studied using the Monte-Carlo simulation, where we found the impact on performance to be negligible up to a hit rate of  $\sim 1 \text{ photon}/\text{HAPD}/\text{event}$ , where one event corresponds to 250 ns. A third concern is that background neutron radiation is also a source of SEUs in the front-end electronics of the ARICH, which might, in some cases, break the DAQ chain and lower the data-taking efficiency.

In the first three years of operation, from 2019 through 2021, the average increase in the APD leakage current was  $\sim 0.3 \mu\text{A}$ , corresponding to a neutron fluence of  $\sim 1 \times 10^{10} \text{ n}_{\text{eq}}/\text{cm}^2$ ,  $O(100)$  below the tolerable limit. The largest background photon hit rate observed so far was at the level of 0.05 photon/HAPD/event, about a factor of 20 below the rate where performance will degrade noticeably. The rate of SEUs is at present observed to be about one per HAPD per day, and most SEUs are corrected on the fly in firmware [46]. In some cases, nonetheless, the DAQ is halted. While such events are rare at present, further mitigation might have to be considered at increased SuperKEKB luminosity.



## 2.5. TOP

The number of detected Cherenkov photons dictates the particle identification capability of the TOP. The typical number is 20–40 photons/track. To maintain good particle identification performance, it is essential to detect the limited number of photons with high efficiency. However, one serious problem caused by the beam background in the TOP detector is a decrease in detection efficiency due to the degradation of the quantum efficiency (QE) of the MCP-PMTs. Measurements in our test bench showed that the QE degrades as a quadratic function of the accumulated output charge  $\Sigma_Q$  of the MCP-PMT,

$$\text{Relative QE} = 1 - 0.2 \left( \frac{\Sigma_Q}{\tau_{\text{QE}}} \right)^2,$$

where  $\tau_{\text{QE}}$  is the lifetime of the MCP-PMT, defined as the output charge corresponding to a relative QE of 0.8, compared to the initial value [47]. Three types of MCP-PMTs were installed, with the lifetime successfully extended during mass production of the MCP-PMTs. The lifetime, measured in a test bench for a limited number of samples, is 1.1 C/cm<sup>2</sup> on average for the conventional type, 10.5 C/cm<sup>2</sup> on average for the ALD type and at least 13.6 C/cm<sup>2</sup> for the life-extended ALD type [47]. Degraded conventional and ALD MCP-PMTs will be replaced with the life-extended type during LS1 and LS2, respectively, for the TOP to withstand higher background rates.

The accumulated output charge is dominated by background Cherenkov photons from electrons and positrons generated when gamma rays hit the quartz bar, and Compton scatter or pair produce. To keep the accumulated output charge of the MCP-PMTs below the expected lifetime until their replacement or the end of Belle II, we have imposed operational limits on the average MCP-PMT hit rate. The exact limit was updated from time to time based on QE projections. In 2021, the limit was 3.0 MHz/PMT. The latest limit, in June 2022, was 5.0 MHz/PMT for single-beam background, with an additional allowance for luminosity term, which cannot be mitigated by varying machine settings or collimators, and which scales with instantaneous luminosity as 0.925 MHz/PMT per  $1 \times 10^{35} \text{ cm}^{-2} \text{ s}^{-1}$ . The TOP MCP-PMT rate limit is the most stringent background limit among the Belle II detector sub-systems, but has not limited accelerator operation with the typical average TOP background rate of about 2 MHz/PMT in 2021.

In addition to the background hits in MCP-PMTs, we have observed that neutron backgrounds cause SEUs in the TOP front-end electronics boards. We have implemented an automated function to detect and correct the SEUs that occur in the configuration memory of programmable logic devices. Unfortunately, this function cannot correct errors that occur in bursts, as multiple simultaneous bit errors cannot be repaired. Such errors account for approximately 1% of all detected errors. Furthermore, the function cannot detect SEUs that occur outside of configuration memory in the on-chip processor, as opposed to the programmable logic. Such errors occasionally occur in critical regions that can halt data taking until the front-end board is power cycled. In 2021 and 2022, manual interventions needed

to recover such boards occurred at a rate of about 5 times a day, which was acceptable in terms of the active channel efficiency. However, a future rise in neutron backgrounds from higher beam currents could be a concern, as it would lead to more frequent halts of the readout boards.

## 2.6. ECL

The ECL detector is robust against backgrounds and does not have a hard background rate limit. However, its energy resolution slowly degrades as background rates increase. A dedicated ECL analysis is still in development.

## 2.7. KLM

The highest occupancy in the KLM occurs in the barrel's inner layers and the endcaps' outer layers. Although there is no significant difference between RPCs and scintillators in the current particle-identification performance, the scintillators are much more robust against backgrounds. The maximum rate limitations of KLM scintillators are being studied [17]. The long dead time of the RPCs during the recovery of the electric field after a discharge significantly reduces the detection efficiency under high background rates. Thus, this expected behavior was addressed in the design by instrumenting the two inner-most layers of the barrel and all layers of the endcaps with scintillators, while re-using RPCs from Belle for the 13 remaining barrel layers. The inner Belle II sub-detectors effectively shield the inner KLM layers and reduce backgrounds produced inside the detector volume. Backgrounds originating outside Belle II in the accelerator tunnel typically penetrate the outer KLM endcap layers first.

The most relevant background sources for the KLM are cosmic muons, fast neutrons produced by single-beam losses and radiative Bhabha scattering at low opening angles [22], and electronics noise. The spring 2021 background level of up to 50 Hz/cm<sup>2</sup> so far has not affected the performance of the KLM. It is planned to readout the signal waveform of the scintillators in the future to provide a higher-resolution (< 1 ns) time measurement than is possible with the existing latch (binary) readout [17]. However, the new firmware will not be able to tolerate the occupancy observed in individual channels, especially for the outer endcap layers. A simpler readout mode for the affected region can be used to cope with this issue. Moreover, additional neutron shielding around Belle II, planned for LS1, should suppress the flux of neutrons hitting the KLM and reduce the detector occupancy.

## 2.8. Recent detector performance degradation

In 2022, before the beginning of LS1, we gradually increased beam currents above 1 A to reach a luminosity higher than  $3 \times 10^{34} \text{ cm}^{-2} \text{ s}^{-1}$ . In this period, several collimators were severely damaged by sudden beam losses, as introduced in Section 1. Because beams incident on the damaged collimator jaw tips can lead to very high backgrounds, several damaged collimators had to be operated with wider apertures than optimal, resulting in a higher beam-induced backgrounds in Belle II. This

background increase caused noticeable reconstruction performance degradation in Belle II, which is remarkable, as the rates, strictly speaking, were still well below the detector limits discussed above. The reduced performance in 2022 thus serves as a preview of the challenges Belle II will face as luminosity and backgrounds increase, and highlights that despite careful simulation and component-level test-beam studies, there are likely to be a number of unanticipated detector-level, system-level, and software-level problems that only arise as backgrounds increase. The collaboration thus must remain vigilant and devote sufficient effort to understanding and mitigating backgrounds, as well as their impact on performance. Crucially, this must include background-level-dependent reconstruction algorithms and calibrations.

Here, we selectively mention some observations of performance degradation caused mainly by increased injection backgrounds due to damaged collimators and by injection chain imperfections at high beam currents. Although the direct impact of the injection background on the data acquisition is suppressed by applying a trigger veto in time with injections, the background can still lead to a noticeable performance degradation up to a few ms after the beam injection. This means that the background level becomes time-dependent, making this a good example of a situation where background-level-dependent reconstruction and calibration will be required.

During 2022 the CDC gain dropped by about 15% over the full detector volume. A drop in gain leads to less charge being collected and, consequently, fewer detected hits. The average number of CDC hits on high momentum tracks in di-muon events and on daughter tracks from  $K_S^0$  was found to decrease by about 12%. This decrease in the number of hits affects the momentum resolution for high-momentum tracks. The reduced collected charge and reduction in hits also lead to a reduction in particle identification performance via  $dE/dx$ , which only partly can be recovered by applying a more sophisticated calibration that takes into account the time of the event since the last injection. Possible causes for the reduced gain include a higher water content than expected in the CDC gas of inner layers, the increased voltage drop across a resistor in HV dividers, space charge effects of slowly moving ions, and faster than expected ageing of the CDC. The resistor mentioned will be replaced during LS1, but an overall quantitative understanding of the gain loss is still missing.

In the same running period, the ECL detector was also noticeably affected by the increased injection background, which is usually off-time and causes a CsI(Tl) crystal pedestal shift due to overlapping of the physics signal pulse ( $\sim 1 \mu\text{s}$ ) with neighboring background events. The shifted pedestal results in underestimated signal pulse height, decreasing the number of crystal hits and, consequently, less effective photon detection and electron identification.

Reduction of the injection background, and mitigation of its impact on performance, will be important tasks going forward. Close collaboration between SuperKEKB and Belle II will be required.

### 3. Background simulation

This section provides a brief overview of the beam-induced background simulation in Belle II. Reference [23] provides a more comprehensive description of most of the Belle II background simulation features implemented to date. A dedicated MC simulation is used to study beam loss processes in the machine, mitigate backgrounds, and evaluate the impact of the possible machine and detector upgrades on backgrounds. As introduced in Section 1, the two dominant classes of beam backgrounds originating from the machine are i) single-beam backgrounds, from circulating charges in individual rings, and ii) luminosity backgrounds, from beam collisions. The simulation proceeds in two steps. First, we perform multi-turn tracking of electrons and positrons in the machine, collecting beam losses around each ring; then, we run simulations of the lost particle interactions with Belle II to study the detector response to beam losses in the IR.

#### 3.1. Particle tracking in the machine

The single-beam background simulation starts with the multi-turn particle tracking software framework Strategic Accelerator Design (SAD) [48]. SAD tracks scattered particles through a sequence of machine elements. Initialized with beam optics parameters and machine apertures, including collimators and beam pipes, SAD tracks particles for 1000 machine turns and collects beam losses around the ring.

The tracking simulation starts by defining a set of  $\sim 500$  equidistant scattering regions around each ring, where bunches of particles are created. These particles are randomly generated within the 3D volume of Gaussian bunches. The momentum and statistical weight of each particle are determined using well-known scattering theories:

- *Coulomb scattering* is described by Rutherford’s scattering formula, including a cutoff Coulomb potential and a screening effect for small angles [25, 49].
- *Bremsstrahlung* follows Bethe-Heitler’s theory in Koch-Motz’s description of complete screening in the Born approximation [50, 51].
- *Touschek scattering* is implemented through Moller’s non-relativistic differential cross section [52] using Bruck’s formula [53] for the loss rate calculation.

All tracked particles in SAD are scattered according to these processes. These stray particles are defined as lost if their spatial coordinates exceed the physical aperture of the machine.

##### 3.1.1. Collimators

Collimators are the narrowest-aperture elements of the machine. They aim to protect sensitive elements of the accelerator and detector by absorbing the beam halo formed mainly by stray particles. Therefore, their accurate implementation into the particle tracking code is crucial.

Recently, the simulation of the SuperKEKB collimation system description was significantly improved [23] compared to

Phase 1 and Phase 2 studies. By default in SAD, machine apertures, including collimators, are modeled as elliptical windows. Outside these windows, particles are considered as lost. This approximation is quite accurate for *KEKB-type* collimators inherited from the KEBK collider. However, *SuperKEKB-type* collimators have two opposite jaws with a rectangular shape and much thinner collimator heads ( $\leq 10$  mm) along the beam axis. Therefore, a refined physical description of *SuperKEKB-type* collimators, and a new simulation of the beam particle interaction with the collimator materials, was implemented. Figure 5 shows the simulated distribution of beam particles lost at a horizontal collimator in the LER. The two black, dot-dashed rectangles show the newly implemented, more realistic collimator edge. Particles passing outside of the rectangular collimator jaws, labelled as “Keep tracking”, are no longer (incorrectly) stopped by the simulated collimator, and instead remain in the simulated beam for tracking. This is a pivotal modification that substantially improved the simulation accuracy, as quantified by ratios between the experiment (Data) and simulation (MC), see next sections.

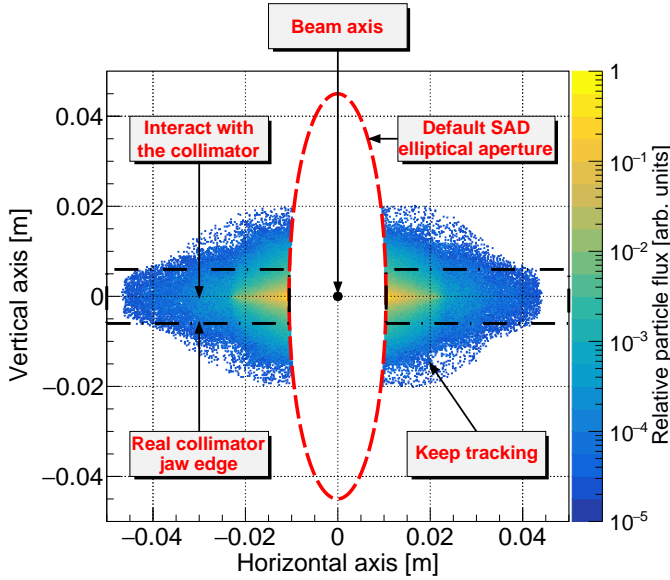


Figure 5: Distribution of beam particles stopped by the LER D06H1 horizontal collimator (red dashed ellipse) in the original SAD simulation. The bin size is  $0.2 \text{ mm} \times 0.2 \text{ mm}$ . Adapted from Ref. [23].

Moreover, for the background studies discussed in this paper, in addition to the introduced improvements in Ref. [23], we have recently implemented particle interaction with the copper collimator chamber. Although these improvements do not change the simulation results for the IR beam losses, they make our simulation code more reliable.

### 3.1.2. Pressure weighting

We describe an improved beam-gas background simulation, which was briefly mentioned in Ref. [23], and uses the measured residual gas pressure distribution. In the initial SAD sim-

ulation for Phase 1 and Phase 2 studies, we assumed a constant and uniform residual vacuum pressure of 1 nTorr in both rings. However, the measured pressure depends both on position (Fig. 6) and time. Therefore, this paper uses the estimated gas pressure to re-weight lost particles depending on their scattering position.

When producing dedicated Belle II Monte-Carlo samples for beam background studies, we typically use fixed reference beam currents ( $I_{\text{LER}} = 1.2 \text{ A}$ ,  $I_{\text{HER}} = 1.0 \text{ A}$ ) which are higher than those achieved during machine operation in 2020 and 2021 ( $I \sim 0.5 \text{ A}$ ), but similar to those achieved in 2022. When the background simulation is validated against measurements, this is done at these reference currents. To facilitate the comparison for the beam-gas background, each lost particle after tracking in SAD is re-weighted by the measured gas pressure at its scattering location around the ring using the CCG gas pressure distribution measured at the time of studies, except that the distribution is initially re-scaled to the reference beam currents.

In order to re-scale the measured CCG gas pressure to the reference beam currents, we study the dependency between the averaged over-the-ring gas pressure as a function of the beam current. Figure 7 shows the average ring pressure ( $\bar{P}$ ) versus beam current ( $I$ ) based on June 2021 CCG measurements. A linear fit, defined as  $\bar{P} = p_0 + p_1 \times I$ , determines i) the base pressure,  $p_0 = \bar{P}(I = 0) = \bar{P}_0$ , which is the average ring pressure when there is no beam, and ii) the average dynamic pressure,  $p_1 \times I = d\bar{P}/dI \times I$ , where  $d\bar{P}/dI$  is the average pressure increase per unit current, physically caused by gas molecules being released from the inner beam pipe walls. The obtained fit parameters are listed in Table 1.

The measured vacuum pressure versus position is then re-scaled to the simulated beam currents (Fig. 6) as follows:

$$P_{\text{CCG},i}^{\text{est.}} = P_{\text{CCG},i}^{\text{meas.}} \times \frac{p_0 + p_1 \times I}{\bar{P}_{\text{CCG}}^{\text{meas.}}}, \quad (2)$$

where  $P_{\text{CCG},i}^{\text{est.}}$  and  $P_{\text{CCG},i}^{\text{meas.}}$  are the estimated and measured gas pressure at the  $i$ -th CCG, respectively, while  $\bar{P}_{\text{CCG}}^{\text{meas.}}$  is the ring averaged pressure.

Although the sensitivities of the pressure gauges are limited to about  $1 \times 10^{-8} \text{ Pa}$ , the scaling helps estimate the pressure below that limit at  $I = 0 \text{ A}$ . Moreover, for the ring-averaged gas pressure calculation in Fig. 7, we consider the saturated value ( $1 \times 10^{-8} \text{ Pa}$ ) as a real measured pressure at the given beam current. Therefore, this assumption leads to overestimated base and underestimated dynamic average pressure in the HER. The peaky, non-uniform distribution of the residual gas pressure in Fig. 6 results in an unequal contribution of lost particles to beam losses depending on their scattered location around the ring.

### 3.2. Particle interactions with the detector

We use the Geant4 (v10.6.3) toolkit [54, 55, 56] embedded into the Belle II Analysis Software Framework (basf2) [57, 58] to simulate the detector response to beam-induced backgrounds using the FTFP\_BERT\_HP Geant4 physics list [59]. Beam-gas and Touschek scattered particles lost near Belle II in SAD are passed from SAD to Geant4 at the inner surface of beam

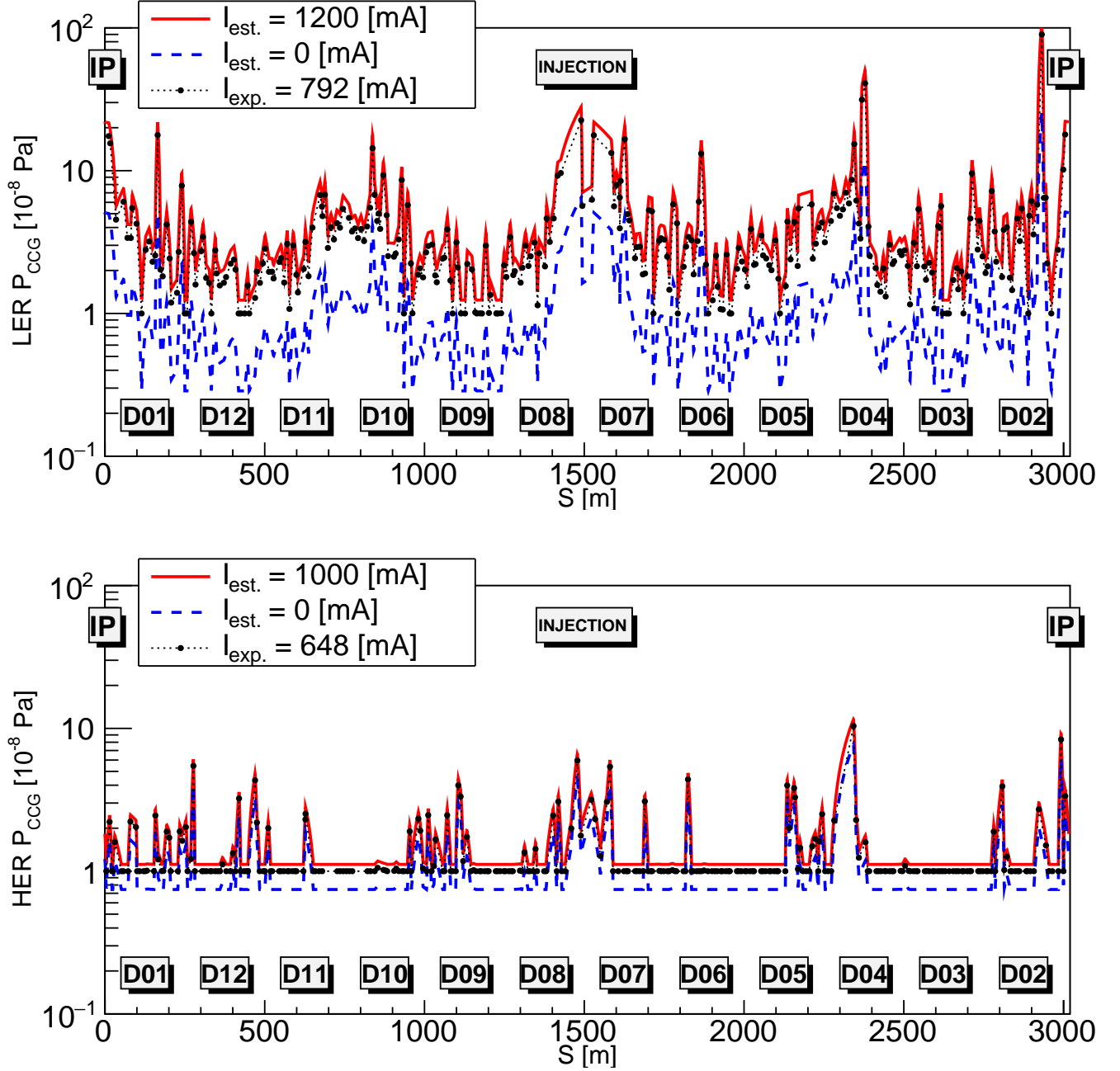


Figure 6: Residual gas pressure versus longitudinal position in the LER (top) and HER (bottom). The black, dotted line with black data points ( $I_{\text{exp.}}$ ) shows pressure measured by CCGs in June 2021. The red, solid and blue, dashed lines ( $I_{\text{est.}}$ ) show estimated pressure at the beam currents listed in the legend. Labels identify different parts of the machine, such as the IP, the IR and the twelve sections of each ring, referred to as D01 through D12.



Table 1: Base ( $p_0$ ) and dynamic ( $p_1$ ) fit parameters of the measured gas pressure averaged over all CCGs as a function of beam currents, see Fig. 7.

Date	$p_0$ [nPa]		$p_1$ [nPa/A]	
	LER	HER	LER	HER
May, 2020	$14.77 \pm 0.01$	$9.47 \pm 0.01$	$52.08 \pm 0.06$	$9.42 \pm 0.01$
June, 2020	$13.23 \pm 0.02$	$9.34 \pm 0.01$	$35.43 \pm 0.10$	$8.51 \pm 0.02$
June, 2021	$11.74 \pm 0.01$	$10.18 \pm 0.01$	$32.48 \pm 0.01$	$5.08 \pm 0.01$
December, 2021	$7.35 \pm 0.07$	$9.13 \pm 0.01$	$37.98 \pm 0.10$	$5.16 \pm 0.01$

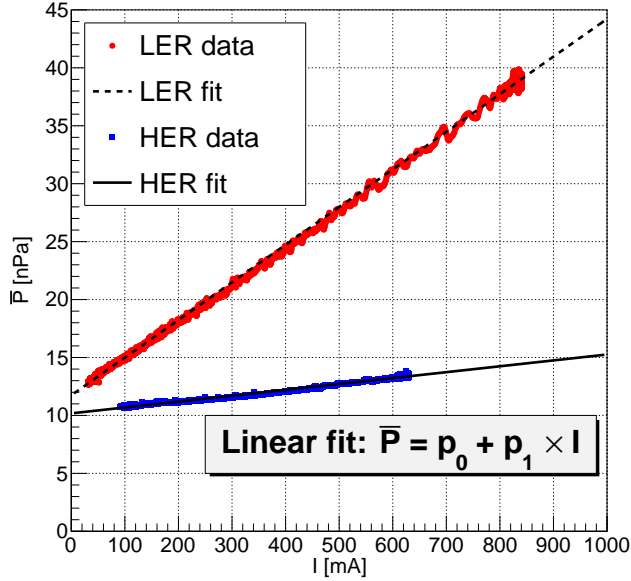


Figure 7: Average ring gas pressure versus beam current measured in June 2021.

pipes and collimators. We have recently improved the SAD to Geant4 interface in order to accurately account for the curvature of beam pipes and the tapered shapes of collimators. The Geant4-simulated region extends out longitudinally  $\sim 30$  m on both sides of the IP. The geometry consists of the IR ( $\pm 4$  m), where Belle II is located, and the so-called *far beamline region*, immediately outside the IR, where the Geant4 geometry includes elements such as magnets, beam pipes, tunnel walls, collimators, and shielding, see Fig. 8. We invested much effort in improving the IR and far beamline geometry description in Geant4. This has made our simulation more consistent with measurements and hence more reliable.

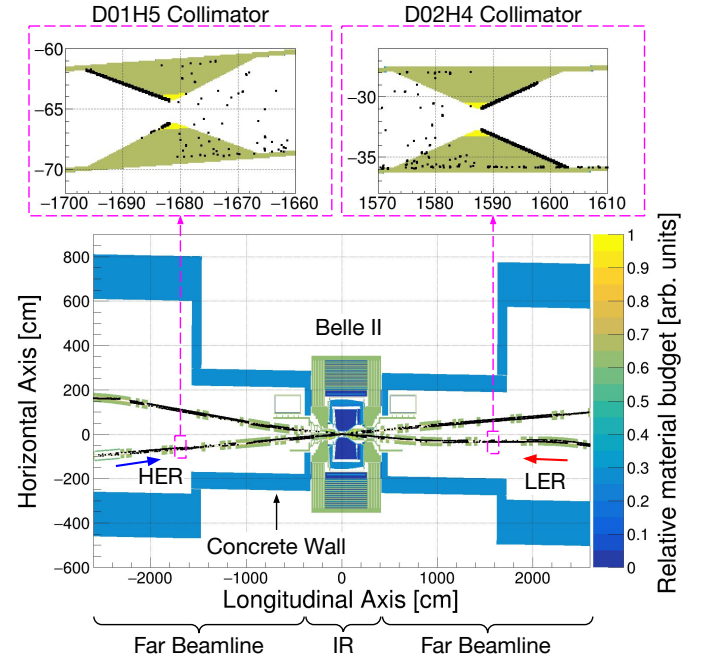


Figure 8: Simulated beam losses on internal surfaces of beam pipe walls. Two top figures show beam loss distribution on upstream surfaces of horizontal collimators.

The luminosity background is simulated using dedicated event generators, followed by Geant4, and the same geometry as described above. SAD is not required in this case. Luminosity backgrounds considered include radiative Bhabha and two-photon processes (Section 1). The specific event generators used are BBBREM [60] and BHWIDE [61] for small ( $< 0.5^\circ$ )

and big ( $> 0.5^\circ$ ) scattering angle radiative Bhabha processes, respectively, and AAFH [62] for two-photon processes.

At the end of the simulation, we collect detector hits for each sub-system of Belle II and compare the simulated against measured background observables.

#### 4. Background decomposition procedure

Here, we give an overview of how the beam-induced background composition at SuperKEKB is measured and modeled. Table 2 lists sub-detector elements and related background observables used for the analysis.

Table 2: Belle II background observables. The twelve diamond detectors (4 QCS-FWD, 4 QCS-BWD, 4 BP) are shown as blue rectangles in Fig. 4.

Sub-detector	Element	Observable	Units
Diamonds	12 detectors	Dose rate	mrads/s
PXD	40 modules	Occupancy	%
SVD	4 layers	Occupancy	%
CDC	56 layers	Hit rate	kHz/wire
TOP	16 slots	Hit rate	MHz/PMT
ARICH	18 segments	Photon rate	MHz/HAPD
KLM	41 layers	Hit rate	MHz/layer

##### 4.1. Background models

###### 4.1.1. Single-beam

In Belle II, the two main single-beam background components are due to beam-gas and Touschek scattering of circulating charges in the vacuum beam pipe. To disentangle these two sources of particle losses, we employ a so-called *heuristic* model, which was first introduced in Phase 1 [10], improved in Phase 2 [11], and further refined here. Following the beam-gas and Touschek scattering theories [4, 25, 63], we model measured observables, largely Belle II detector rates and occupancies (Table 2), as

$$O_{\text{beam-gas}} = B \times I \bar{P}_{\text{eff.}}, \quad (3)$$

$$O_{\text{Touschek}} = T \times \frac{I^2}{n_b \sigma_x \sigma_y \sigma_z}, \quad (4)$$

where  $O_{\text{beam-gas}}$  ( $O_{\text{Touschek}}$ ) is the beam-gas (Touschek) component;  $B$  ( $T$ ) is the beam-gas (Touschek) sensitivity,  $I$ ,  $\bar{P}_{\text{eff.}}$  and  $n_b$  are the beam current, the ring average effective residual gas pressure seen by the beam, and the number of bunches in each ring, respectively. The bunch volume is defined by the product of  $\sigma_x$ ,  $\sigma_y$ , and  $\sigma_z$ , which are bunch sizes in the XY-plane and bunch length along the beam axis, respectively.

While the transverse bunch sizes are measured continuously during background studies, the longitudinal bunch length is not.

Therefore, we instead parameterize the bunch length dependence on other beam parameters. Measurements of this dependence in commissioning Phase 3 are discussed further in Ref. [64]. For our analysis, we use updated results [65] performed in 2020 and 2021 for the HER and LER, respectively. In our fit model, the bunch length is parameterized as follows:

$$\sigma_z^{\text{LER}} [\text{mm}] = 5.4466 + 1.7642 \times \frac{I^{\text{LER}} [\text{mA}]}{n_b^{\text{LER}}}, \quad (5)$$

$$\sigma_z^{\text{HER}} [\text{mm}] = 6.0211 + 1.3711 \times \frac{I^{\text{HER}} [\text{mA}]}{n_b^{\text{HER}}}. \quad (6)$$

During machine operation, there is a constant flow of desorbed gas from the beam pipe to the vacuum pumps. As a result of this flow, the finite conductance of the vacuum system and the location of the CCGs, the ring average pressure at center of the beam pipe,  $\bar{P}_{\text{eff.}}$ , which is the pressure relevant for beam-gas scattering, is higher than the pressure measured by CCGs. We use the CCG data to estimate  $\bar{P}_{\text{eff.}}$ . It is assumed, based on geometry, that the dynamic pressure measured by CCGs,  $I(d\bar{P}/dI)_{\text{CCG}}$ , is three times lower than at the center of the beam pipe, while the base pressure,  $\bar{P}_{0,\text{CCG}}$ , is assumed to be the same as seen by the beam. Therefore,  $\bar{P}_{\text{eff.}}$  can be obtained from the measured CCG gas pressure averaged over the ring as follows

$$\bar{P}_{\text{eff.}} = 3I(d\bar{P}/dI)_{\text{CCG}} + \bar{P}_{0,\text{CCG}} = 3\bar{P}_{\text{CCG}} - 2\bar{P}_{0,\text{CCG}}, \quad (7)$$

where  $\bar{P}_{\text{CCG}} = I(d\bar{P}/dI)_{\text{CCG}} + \bar{P}_{0,\text{CCG}}$  as discussed in Section 3.1.2. Table 3 lists extrapolation parameters of  $\bar{P}_{\text{eff.}}$  as a function of beam currents for so-called *sensing* ring sections, where the measured CCG pressure averaged over the ring section behaves linearly along the full range of the measured beam current (10–1000 mA) above the CCG hardware limit of 10 nPa. In Table 3, the averaging over the ring before fitting is done as an arithmetic mean over the ring sections specified in the second and third columns for the LER and HER, respectively. The parameters are used for Data/MC calculation, where  $\bar{P}_{\text{eff.}}$  is extrapolated towards simulated beam currents, see later in the text.

The overall single-beam background observable for each ring is defined as a sum of beam-gas ( $O_{\text{beam-gas}}$ ) and Touschek ( $O_{\text{Touschek}}$ ) components plus a constant pedestal ( $D$ ) which represents the detector electronics noise or calibration offset

$$O_{\text{single}} = B \times I \bar{P}_{\text{eff.}} + T \times \frac{I^2}{n_b \sigma_x \sigma_y \sigma_z} + D, \quad (8)$$

where  $\bar{P}_{\text{eff.}}$  is defined in Eq. (7) with  $\bar{P}_{\text{CCG}}$  calculated as an average CCG gas pressure over sensing ring sections, and  $\bar{P}_{0,\text{CCG}}$  taken from Table 3, assuming the base pressure stays stable during the study.

During the early stage of the commissioning Phase 3, a large photon background was observed for some runs in a few modules of the PXD detector. Since the interaction region is designed so that no direct SR photons hit the central beam pipe, most of the SR background consists of secondary photons. To

Table 3: Base ( $\bar{P}_{0,\text{CCG}}$ ) and dynamic ( $(d\bar{P}/dI)_{\text{CCG}}$ ) fit parameters of the measured CCG gas pressure averaged over sensing ring sections as a function of beam currents.

Date	Sensing ring sections		$\bar{P}_{0,\text{CCG}}$ [nPa]		$(d\bar{P}/dI)_{\text{CCG}}$ [nPa/A]	
	LER	HER	LER	HER	LER	HER
May, 2020	D01-D12	D02, D04, D09	$14.79 \pm 0.22$	$9.66 \pm 0.58$	$52.08 \pm 1.25$	$11.54 \pm 1.44$
June, 2020	D01-D12	D02, D04, D09	$13.07 \pm 0.44$	$10.13 \pm 0.79$	$36.23 \pm 2.00$	$9.77 \pm 2.04$
June, 2021	D01-D11	D02, D04, D09, D12	$12.68 \pm 0.16$	$10.72 \pm 0.04$	$30.55 \pm 0.57$	$6.24 \pm 0.08$
December, 2021	D01-D11	D02, D04, D12	$7.92 \pm 0.95$	$10.52 \pm 0.03$	$39.76 \pm 1.42$	$5.40 \pm 0.04$

account for the SR background in our model,  $O_{\text{SR}}$ , which is proportional to the HER beam current, we extend the HER heuristic fit formula for the PXD detector as follows

$$O_{\text{single}}^{\text{PXD}} = O_{\text{single}} + S \times I, \quad (9)$$

where  $S$  is the SR sensitivity.

#### 4.1.2. Luminosity

The luminosity background is, by definition, linearly proportional to the instantaneous luminosity ( $\mathcal{L}$ ). We describe this background component as follows

$$O_{\text{lumi}} = L \times \mathcal{L}, \quad (10)$$

where  $L$  is the luminosity sensitivity. The luminosity background can be evaluated from measured observables,  $O_{\text{meas.}}$ , during collisions by subtracting single-beam backgrounds from non-injection data:

$$O_{\text{lumi}} = O_{\text{meas.}} - (B \times I \bar{P}_{\text{eff.}} + T \times \frac{I^2}{n_b \sigma_x \sigma_y \sigma_z})^{\text{LER}} - (B \times I \bar{P}_{\text{eff.}} + T \times \frac{I^2}{n_b \sigma_x \sigma_y \sigma_z})^{\text{HER}} - \frac{1}{2}(D^{\text{LER}} + D^{\text{HER}}). \quad (11)$$

Note that for each individual sub-detector element, there are specific observables listed in Table 2 and sensitivities:  $B^{\text{LER,HER}}$ ,  $T^{\text{LER,HER}}$ ,  $D^{\text{LER,HER}}$ , and  $L$ , plus  $S^{\text{HER}}$  for the PXD SR background.

#### 4.2. Dedicated background studies

Approximately twice a year, the Belle II beam background group performs dedicated beam-induced background measurements at SuperKEKB. The major goals are to investigate the background composition and to compare measurements against simulation. This information is needed to make reliable projections of future backgrounds and to perform targeted background mitigation. We focus on four comprehensive studies under stable and well-controlled machine conditions, which were conducted on May 9 ( $\beta_y^* = 1.0$  mm) and June 27 ( $\beta_y^* = 0.8$  mm)

in 2020, and June 16 ( $\beta_y^* = 1.0$  mm) and December 20 ( $\beta_y^* = 1.0$  mm) in 2021.

Figure 9 illustrates the study performed on May 9, 2020. The top plot shows an example of one background observable, a measured diamond detector dose rate (open gray circles). The bottom plot shows measured beam parameters. The study consists of three types of measurements identified in the top plot: i) no-beam (#1), to estimate statistical fluctuation of the measured observable without beams circulating in the machine; ii) single-beam (#2 LER, #3 HER), where one ring at a time is filled with a beam of particles; iii) luminosity (#4-6), to study beam losses during collisions of the two beams. For the single-beam background measurements, we inject only one beam to a current of  $\sim 0.5$  A and collect data during about 5 min of top-up injections. This allows the gas pressure to settle and provides data for the study of the injection background. Then, the beam current is left to decay for about 15 min with no injection. This data sample is defined as *beam decay* and shown as hatched bands in Fig. 9 (bottom). Varying the number of bunches in the ring allows us to disentangle the beam-gas and Touschek components, as only the latter depends on the number of bunches at fixed beam current, see Eq. (4). We use Eq. (8) to fit measured observables during the single-beam study for each ring separately, which yields background sensitivities for the beam-gas ( $B^{\text{LER,HER}}$ ) and Touschek ( $T^{\text{LER,HER}}$ ) components, as well as detector pedestal ( $D^{\text{LER,HER}}$ ). The single-beam fit results, see hatched areas in Fig. 9 (top, where the LER and HER extrapolated backgrounds are shown as stacked histograms), can then be extrapolated to other times using machine parameters and are used in the following luminosity background measurements. To study luminosity backgrounds for a fixed number of bunches, we 1) scan the luminosity during top-up injection for both beams at nominal currents (#4) by applying a vertical orbit offset between the colliding beams, and then 2) stop injection, leaving both beams to decay (#5 and #6). The luminosity background (open black squares) is calculated as the difference between non-injection data (open green triangles) collected during periods 1) and 2) and the sum of the extrapolated LER and HER single-beam heuristic fits, see Fig. 9.

Figure 10 shows the luminosity background versus the collision luminosity, measured by the ECL as explained in Section 1, for the top-up injection period (#4, solid black stars) and the two beam decays (#5, solid blue squares, and #6, solid

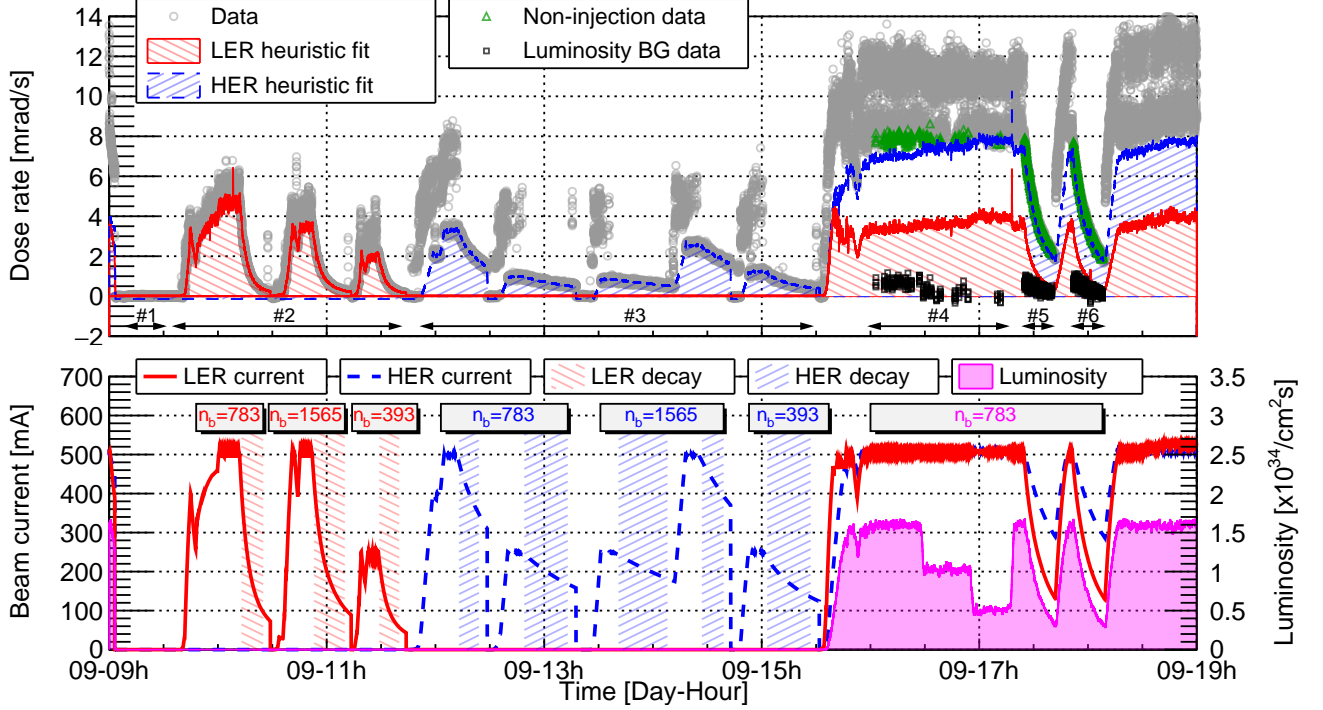


Figure 9: Example of dedicated beam background measurements on May 9, 2020. Top: BP-FW-325 diamond detector dose rate; bottom: SuperKEKB machine parameters. See text for detailed discussion.

red triangles). As expected, these three distributions illustrate a clear linear dependency between the luminosity background ( $O_{\text{lumi}}$ ) and the instantaneous luminosity ( $\mathcal{L}$ ). We fit the estimated luminosity background versus luminosity with a first-order polynomial, as shown in Fig. 10. In the absence of any residual systematic effects, we would expect all three fits to go through the origin and to have very similar slopes. For the particular Diamond detector shown in Fig. 10, this is the case for the fits to data sets #5 and #6. The fit to data set #4, however, has a different slope and a negative intercept with the vertical axis, which would correspond to negative luminosity background and is unphysical. We speculate that for this detector, data set #4 is biased by a residual contribution of the injection background that leaks into our estimated non-injection background. In addition, our analysis implicitly assumes that the non-luminosity background sensitivities are the same during single-beam and collision modes of the accelerator. If this assumption does not hold, offsets such as observed in data set #4 are also possible. To account for these uncertainties, the final luminosity background extrapolation for all detectors discussed in the text below generally uses the average slope of three linear fits analogous to those shown in Fig. 10, with the caveat that fits with negative slope are discarded. For each detector, we assign a systematic uncertainty equal to the average of the three (or fewer, if some of the fits are discarded) intercepts with the vertical axis.

#### 4.3. Injection background

SuperKEKB requires continuous injection of particles to keep the beam currents constant and luminosity high. Beam

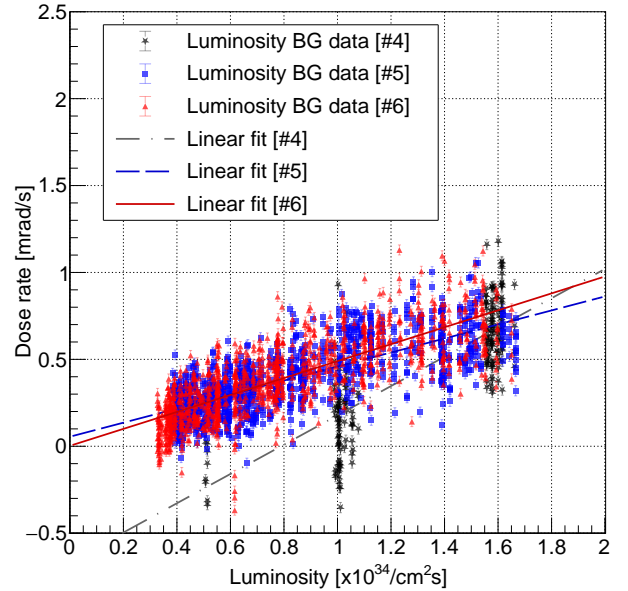


Figure 10: Luminosity component of the measured BP-FW-325 diamond detector dose rate versus instantaneous luminosity from the May 9, 2020 study.



losses in the IR can increase for a short period of time, typically  $O(10\text{ ms})$ , after injection, which can be detrimental to both detector operations and reconstruction performance. In order to avoid DAQ saturation, a L1-trigger veto rejects triggers that occur close to the time when a newly injected bunch passes the IP. Therefore, in most detectors only the part of the injection background that is outside the L1-trigger veto is seen as an excess over the storage (non-injection) background. However, vetoed events will still contribute to the dose rate seen by detectors, and hence must be included in dose rate estimates. Prediction of the injection background via simulation is a very challenging task, as it depends on a broad spectrum of machine parameters, all the way from the particle gun and LINAC to the injector and stored beam.

Below, we compare two methods under development to estimate the SuperKEKB injection background in Belle II experimental data.

#### 4.3.1. Background remnant

One straightforward approach to estimating the injection background ( $O_{\text{inj.}}$ ) is to use the heuristic fit results described above. We subtract the estimated storage background ( $O_{\text{est.}}$ ) from measured data ( $O_{\text{meas.}}$ ) during a top-up injection period of 5 min before each beam decay.

Figure 11 illustrates the measured background for the SVD L3 during the HER single-beam top-up injection. The upper part of the figure shows the HER beam current with 1174 bunches of electrons. The bottom part of the figure contains two data sets of the measured mean occupancy with a timestamp of 1 Hz for outside (black, solid circles) and inside (red, open circles) the injection veto window. The blue, hatched area represents the estimated HER storage background extrapolated by using heuristic fit results ( $O_{\text{single}}^{\text{HER}}$ ). Seven beam injection periods occur in this figure, where the 1-bunch injection repetition rate is 12.5 Hz. One of the injection periods is highlighted by a vertical orange band. The subsequent beam decay period is highlighted in cyan. The frequency of injection periods depends on the beam lifetime and the maximum acceptable beam current drop, typically set at 1% of the operational current. The figure is a good illustration of the injection trigger veto performance. The trigger system vetoes high beam losses for about 10 ms right after the beam injection inside the veto window to ensure stable DAQ operation. When the injection is stopped, the beam current decays (vertical cyan band in the figure), and the observed background is presumably due to the storage beam circulating in the ring.

To estimate the full radiation dose (and hence the potential for radiation damage of electronics) on Belle II sub-detectors, the contribution from injection background, including the component *hidden* by the L1-trigger injection veto, must be included. Data inside the trigger veto window is affected by the DAQ dead time fraction due to the veto,  $F_{\text{DT}} \sim 3 - 6\%$ . Furthermore, we only inject the beam some fraction of the time (see Fig. 11),  $F_{\text{ID}} \sim 50 - 70\%$ , which is defined as the ratio of the injection duration to the sum of the injection duration and decay duration. Both  $F_{\text{DT}}$  and  $F_{\text{ID}}$  must be accounted for when normalizing the estimated injection background.

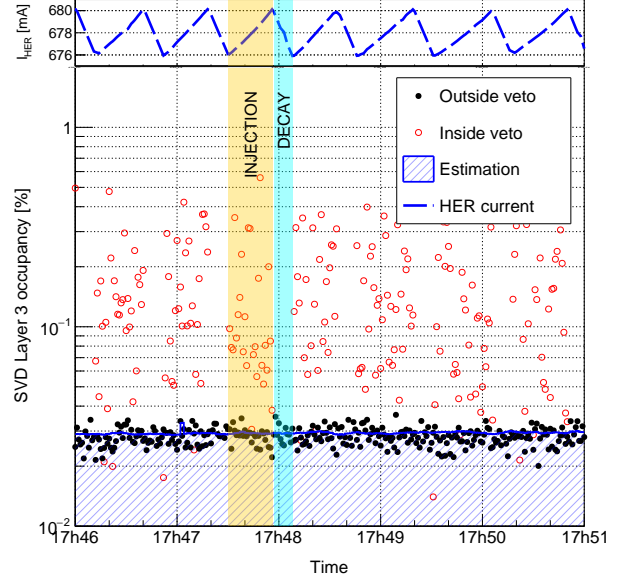


Figure 11: Top: measured HER beam current during top-up injection for June 16, 2021 background studies; bottom: measured occupancy for the innermost SVD layer.

We define the relative injection background as

$$\tilde{O}_{\text{inj.}} = O_{\text{inj.}}/O_{\text{est.}} = (O_{\text{meas.}} - O_{\text{est.}})/O_{\text{est.}} \quad (12)$$

Since the injection background is seen only during a short period when a fresh beam is injected into the main ring, each data point in Fig. 11 is then normalized by  $F_{\text{DT}}$  and  $F_{\text{ID}}$ :

$$\tilde{O}_{\text{inj.}}^{\text{norm.,in}} = \tilde{O}_{\text{inj.}}^{\text{in}} \times F_{\text{DT}} \times F_{\text{ID}}, \quad (13)$$

$$\tilde{O}_{\text{inj.}}^{\text{norm.,out}} = \tilde{O}_{\text{inj.}}^{\text{out}} \times (1 - F_{\text{DT}}) \times F_{\text{ID}}, \quad (14)$$

where  $\tilde{O}_{\text{inj.}}^{\text{norm.}}$  is the normalized injection fraction.

Figure 12 shows the Belle II normalized relative injection background for the June 2021 study, where  $\tilde{O}_{\text{inj.}}^{\text{norm.}}$  varies within one order of magnitude for outside ( $\tilde{O}_{\text{inj.}}^{\text{norm.,out}}$ , solid markers) and inside ( $\tilde{O}_{\text{inj.}}^{\text{norm.,in}}$ , open markers) the injection veto data samples. The sampled beam background data with a timestamp of 100 ms and 1 s for the diamond and TOP detectors, respectively, are collected without the L1-trigger and injection veto. Each data point in Fig. 12 is normalized by the DAQ dead time fraction during the injection and decay periods following Eqs. (13) and (14), respectively. Error bars illustrate the total uncertainty, including statistical and systematic errors, where the latter is calculated as a geometric standard error over all layers in a given sub-detector.

Based on the measured total and estimated storage backgrounds, this method allows us to estimate the injection background during top-up injection in one of the rings. Following this approach, we can evaluate the radiation damage in Belle II

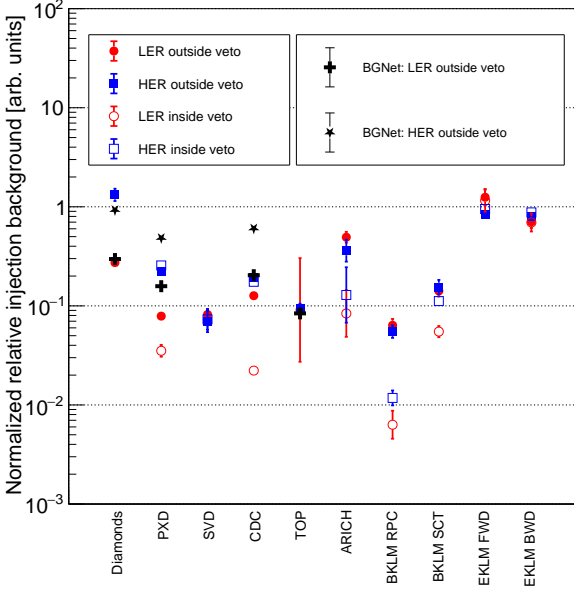


Figure 12: The normalized relative injection background during the June 2021 study. BKLM RPC stands for the barrel KLM layers made of RPCs, BKLM SCT represents barrel KLM scintillator layers, and EKLM FWD and BWD show the relative injection background for the KLM endcaps on the forward and backward sides, respectively, made of scintillator layers.

sub-detectors by integrating the storage and injection background doses, taking the injection trigger veto impact into account, and properly normalising the injection background fraction. However, the main limitation of this method is that the fraction of the injection background does not stay constant for a long time during machine operation due to continuous machine tuning and different beam (bunch) currents and luminosity. Therefore, the results of this injection background estimation can be extrapolated outside the dedicated background study runs only with certain assumptions regarding the ratio between injection and storage background components measured by the detector.

#### 4.3.2. Neural network

BGNet [66] is an artificial neural network for predicting the background rate of Belle II sub-detectors. The network learns to map SuperKEKB collider variables to background hit rates caused by different beam background sources seen by Belle II. One major motivation is to accurately extract background hit rates from top-up injections, understand their dependence on collider conditions, and mitigate their impact on data taking. Feature attribution algorithms [67, 68] are applied to identify the most predictive input variables.

BGNet consists of neural network-based models for the most relevant background sources as the physical origin for the loss of beam particles near the interaction region of Belle II as follows: i) the beam-gas storage background in the LER and HER, ii) the Touschek storage background in the LER and HER, iii) the luminosity background, iv) the LER and HER top-up injection background, and v) detector pedestals. The models

for beam-gas and Touschek contributions to the hit rate follow Eq. (3) and Eq. (4) but replace the coefficients  $B$  and  $T$  by fully connected feed-forward artificial neural networks, respectively. The injection background hit rate network (separately for the HER/LER) is a fully connected feed-forward network multiplied with an injection gate status variable. The injection gate status is open (variable value of 1) whenever top-up injections into a ring take place, otherwise, it is closed (value of 0). The collision and pedestal-related background components are represented by the weight and bias of a linear neuron with the measured luminosity as its only input variable.

BGNet is trained on archived 1 Hz time series of process variables (PVs) provided by the EPICS-based slow-control system of Belle II. The training target is the observed total background hit rate of a Belle II sub-detector. The input tensors for HER/LER injection and storage background networks are selected based on expert knowledge, and the result of feature attribution methods is used to rank the importance of variables. During training, BGNet optimizes the weights and biases of its sub-networks to minimize the mean absolute error between the measured hit rate and the sum over all predicted background components. The data are split into training and validation sets. All input variables and the measured hit rate are scaled by subtracting the median and scaling by the percentile range between the 90th and 10th percentile.

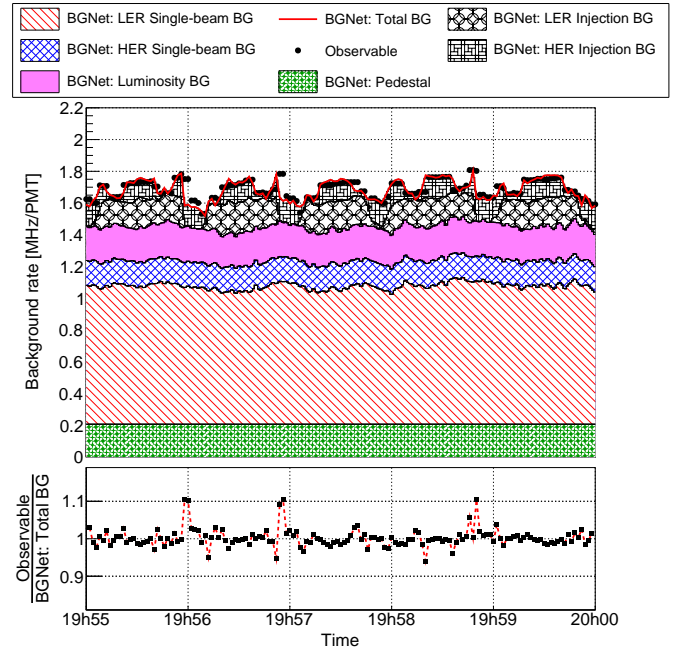


Figure 13: Components of the TOP detector background predicted by BGNet for the June 16, 2021 background study. Top: stacked histograms of predicted background components displayed on top of the observable; bottom: the ratio between the observable and predicted total background.

Figure 12 contains BGNet estimation results for the relative injection background outside the veto. The neural network and heuristic fit results demonstrate an acceptable agreement for the outside veto data. However, there is a noticeable disagreement for some sub-detectors, e.g. for the PXD and CDC, since

BGNet uses the online archived data, which may contain noisy electronics channels that are masked for the heuristic fit offline.

Storage backgrounds (single-beam and luminosity) are learned mostly from beam decay data during single-beam and collision operation of the collider. During physics runs, the injection backgrounds show a typical temporal pattern following the injection gate status in the HER and LER since the top-up injections regularly paused and resumed to keep the beam currents constant, as shown in Fig. 13, which corresponds to the following beam parameters:  $I^{\text{LER/HER}} = 740/650$  mA,  $n_b = 1174$ , and  $\mathcal{L} = 2.6 \times 10^{34} \text{ cm}^{-2} \text{ s}^{-1}$ . The injections into the HER and LER are asynchronous. The contribution of HER and LER injections can be disentangled even during physics runs by looking at the beam gate status variables.

The BGNet was tested on recorded data during Belle II operation in 2021 and 2022. After training, the model learned a physically sensible and accurate decomposition of the detector observables into components for different background sources. In addition, feature attribution algorithms have been applied to the sub-models in BGNet to understand which inputs the sub-models find most valuable for making predictions. The method can provide valuable clues to understand the backgrounds in Belle II better. We are working on further developing the neural network to make it a helpful tool used by SuperKEKB operators for crucial machine parameter tuning, to mitigate backgrounds, or to improve collider performance.

## 5. Summary of the measured background composition

This section summarizes the background status in Belle II as of June 2021, reporting on our current understanding of beam-induced backgrounds. At that time, the detector was running with stable machine operation with well-controlled and understood beam backgrounds, in contrast to 2022 operation with frequent sudden beam losses and damaged collimators. We also compare background measurements against dedicated simulations.

### 5.1. Measured backgrounds

Table 4 shows detector limits. The TOP limit before LS1 is related to the replacement of TOP conventional PMTs planned for LS1. At the same time, the limit after LS1 is associated with the replacement of ALD PMTs in LS2 and the longevity of life-extended ALD PMTs. Moreover, the upper background rate limit quoted for the Diamond read-out electronics can be increased by selecting a lower signal amplification. The KLM detector limit corresponds to the muon reconstruction efficiency drop of about 10%.

The estimated future background in Table 4 is the main goal of this article, and obtaining this requires knowledge of the detailed background composition and good Data/MC agreement. These topics will be detailed in what follows.

Figure 14 shows the measured background rate and composition (i.e. decomposed by the most significant beam loss sources) for each Belle II sub-system separately. The data used are from the luminosity background study on

June 16, 2021 at the following beam condition:  $I^{\text{LER/HER}} = 732.6/647.2$  mA,  $n_b = 1174$ ,  $\sigma_x^{\text{LER/HER}} = 184.6/151.0 \mu\text{m}$ ,  $\sigma_y^{\text{LER/HER}} = 60.7/36.2 \mu\text{m}$ ,  $\sigma_z^{\text{LER/HER}} = 6.5/6.8$  mm,  $P_{\text{eff}}^{\text{LER/HER}} = 88.7/24.3$  nPa, and  $\mathcal{L} = 2.6 \times 10^{34} \text{ cm}^{-2} \text{ s}^{-1}$ . Beam-gas, Touschek, luminosity, and PXD SR backgrounds are obtained using the heuristic fit methodology described earlier. The total injection background ( $O_{\text{inj.}}$ ) corresponds to the inside ( $\tilde{O}_{\text{inj.}}^{\text{norm.,in}}$ , Eq.13) and outside ( $\tilde{O}_{\text{inj.}}^{\text{norm.,out}}$ , Eq.14) the veto injection background normalized by the DAQ dead time and injection duration fractions during top-up injection and beam decay:

$$O_{\text{inj.}} = (\tilde{O}_{\text{inj.}}^{\text{norm.,in}} + \tilde{O}_{\text{inj.}}^{\text{norm.,out}}) \times O_{\text{single}}, \quad (15)$$

where  $O_{\text{single}}$  is the estimated single-beam background.

The overall background level for all sub-systems is well below the detector limits listed in Table 4. The dominant backgrounds are due to LER beam-gas, LER Touschek and luminosity beam losses. HER and injection backgrounds are much lower, at the level of 10%, except for the ARICH, which is more sensitive to FWD-directed beam losses from the HER beam. The reported rates are affected by the so-called event-of-doom buster (EoDB), introduced in 2020. The EoDB removes events with more than 6000 hits in the CDC or more than 70 000 digits in the SVD, introducing a systematic bias of about 20% to the measured total background rate during the injection.

At the present level, the SR background is of no concern in terms of occupancy for the inner-most layers of the vertex detector. However, its potential increase at higher beam currents or at different beam orbits tuned to increase the luminosity may cause inhomogeneities in the irradiation of the PXD modules, which is difficult to compensate by simply adjusting the operation voltages of the affected modules.

The neutron background is not considered explicitly in the study reported here. However, the neutron background in the SuperKEKB tunnel near Belle II has been studied separately, using direction and energy-sensitive gas TPC detectors to image neutron recoils [22]. Those results, converted into estimated 1-MeV neutron equivalent fluences per Snowmass year, are listed in Table 5. In addition, Table 6 reports on the current thermal neutron fluxes measured by the  $^3\text{He}$  tube neutron counting system, which were not previously published.

TPC and  $^3\text{He}$  tube results show that LER single-beam backgrounds are the dominant background sources in the FWD tunnel, which could be explained by high beam losses at the nearest, tightly closed collimator  $\sim 16$  m from the IP, see Fig. 8. On the other hand, the BWD tunnel neutrons are predominantly due to luminosity background “hotspots”, which are expected on either side of the Belle II detector [22].

Moreover, the neutrons from the electromagnetic showers, originating from both the IR and accelerator tunnels, might be the reason for SEUs of FPGA electronics boards seen during the beam operation. Our simulation and dedicated machine studies show that beam losses at the collimators nearest to the detector, and thus single-beam neutrons, can be suppressed by aperture adjustment of distant upstream collimators in each ring. However, we can only mitigate the luminosity neutron background by installing additional shielding around the detector. We are

Table 4: Background rate limits for different Belle II detector sub-systems. The third column shows the total measured background rate in June 2021 at  $\mathcal{L} = 2.6 \times 10^{34} \text{ cm}^{-2} \text{ s}^{-1}$  excluding the pedestal rate. The fifth column shows the total estimated background rate before LS2 at  $\mathcal{L} = 2.8 \times 10^{35} \text{ cm}^{-2} \text{ s}^{-1}$ . The TOP luminosity background is assumed to be 0.925 MHz/PMT per  $10^{35} \text{ cm}^{-2} \text{ s}^{-1}$ .

Detector	BG rate limit	Current (June 2021)		Estimated (Before LS2)		
		Background	Safety factor	Background	Safety factor	
Diamonds	1–2 rad/s	< 132 mrad/s	> 17	< 311 mrad/s	> 7.2	
PXD	3%	0.1%	30.1	0.4%	6.9 (L1)	
SVD L3, L4, L5, L6	4.7%, 2.4%, 1.8%, 1.2%	< 0.22%	21.5	1.0%	4.7 (L3)	
CDC	150 kHz/wire	22.3 kHz/wire	6.7	79 kHz/wire	1.9	
ARICH	10 MHz/HAPD	0.5 MHz/HAPD	21.7	1.4 MHz/HAPD	7.3	
Barrel KLM L3	50 MHz	4 MHz	12.1	12 MHz	4.1	
	non-luminosity BG					
	before LS1	after LS1				
TOP	3 MHz/PMT	5 MHz/PMT	1.8 MHz/PMT	1.8	5.0 MHz/PMT	1.5
	+ luminosity BG					

Table 5: The measured fast neutron background by TPCs in the accelerator tunnel at  $\mathcal{L} = 2.6 \times 10^{34} \text{ cm}^{-2} \text{ s}^{-1}$ .

Background type	Accelerator tunnel	Fluence per smy [ $\times 10^8 \text{ n}_{\text{eq}}/\text{cm}^2$ ]
Single-beam	BWD/FWD	6/90
Luminosity	BWD/FWD	40/4

Table 6: The measured thermal neutron background by  $^3\text{He}$  tubes in the accelerator tunnel at  $\mathcal{L} = 2.6 \times 10^{34} \text{ cm}^{-2} \text{ s}^{-1}$ .

Background type	Accelerator tunnel	Flux [ $\times 10^2 \text{ n}/(\text{cm}^2 \text{ s})$ ]
Single-beam	BWD/FWD	1/30
Luminosity	BWD/FWD	20/4

currently working on further neutron background studies, dedicated countermeasures, and possible detector upgrades, which will be discussed in forthcoming publications.

## 5.2. Simulation accuracy

To probe the accuracy of the Belle II background simulation and our current understanding of the major beam loss processes in SuperKEKB, we calculate the Data/MC ratio for the four beam background studies performed in 2020 and 2021 (see Section 4.2). A dedicated set of Monte-Carlo simulations based on SAD and Geant4 is prepared for each study using the procedure discussed in Section 3. Each component of the measured background is then scaled to the simulated beam parameters using the heuristic fit results so that measured and simulated rates can be compared for identical beam parameters. Figure 15 shows a summary of the findings, Belle II detector-level Data/MC ratios, where each value is calculated as a geometric mean over i) the relevant sub-detector’s layers, modules, sensors or segments as discussed in Section 4, and over ii) the four background studies. The statistical uncertainties originate from the heuristic fit parameter errors, while the systematic uncertainties are defined as variations of the individual ratio around the mean value and calculated as a standard error of the geometric mean [69, 70]. The measured and simulated data are compared at arbitrary beam parameters:  $I^{\text{LER/HER}} = 1.2/1.0 \text{ A}$ ,  $n_b = 1576$ ,  $\mathcal{L} = 8 \times 10^{35} \text{ cm}^{-2} \text{ s}^{-1}$ . The average gas pressure is estimated based on reported parameters in Table 3. The combined ratios over all Belle II sub-systems for single-beam and luminosity backgrounds are summarized in Table 7.

As reported in Refs. [10] and [11], agreements between first measurements and optimistic background simulation in 2016 and 2018 were poor, and Data/MC ratios strongly diverged from the unity by several orders of magnitude. Therefore, during



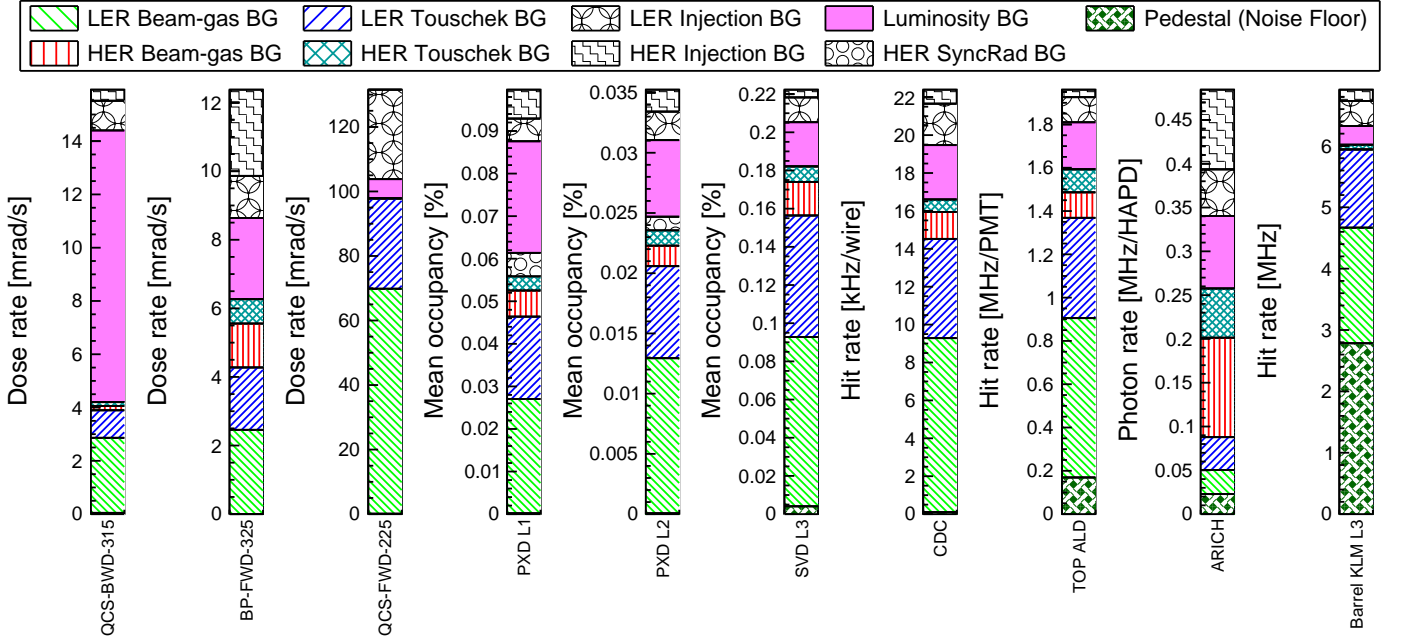


Figure 14: Measured Belle II background composition on June 16, 2021. Each column is a stacked histogram. QCS-BWD-315, BP-FWD-325 and QCS-FWD-225 indicate backward QCS, beam pipe and forward QCS Diamond detectors, respectively, with the higher dose rate. Barrel KLM L3 corresponds to the inner-most RPC layer in the barrel region of the KLM detector. TOP ALD shows the averaged background over ALD-type MCP-PMTs, slots from 3 to 9.

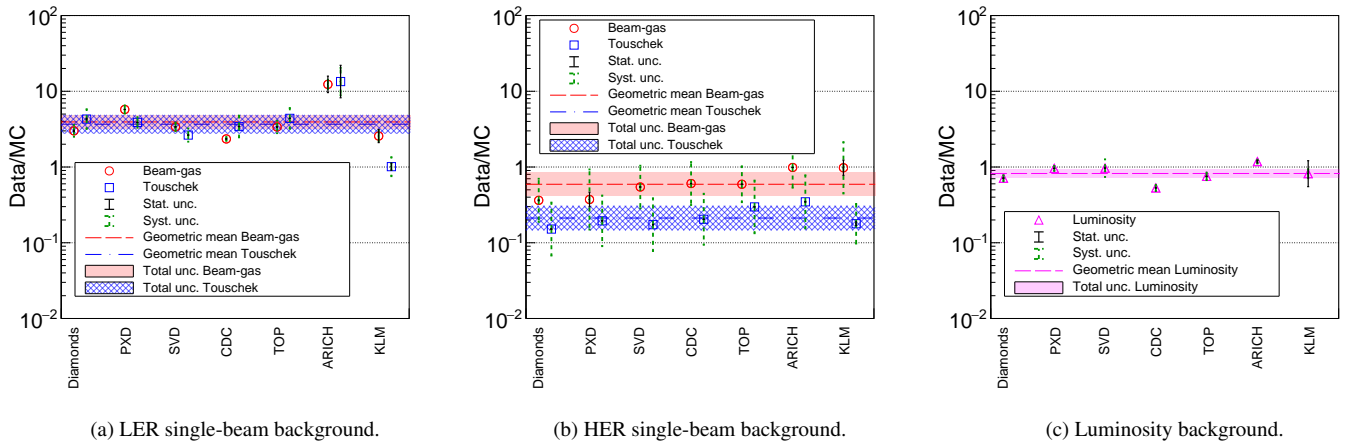


Figure 15: Belle II detector-level Data/MC ratios in Belle II over 2020 and 2021 dedicated background studies.

Table 7: Combined Belle II Data/MC ratios over 2020-2021 collected data.

Background	LER	HER
Beam-Gas	$3.94^{+0.92}_{-0.74}$	$0.59^{+0.25}_{-0.18}$
Touschek	$3.67^{+1.22}_{-0.92}$	$0.21^{+0.10}_{-0.07}$
Luminosity	$0.82^{+0.11}_{-0.10}$	

the early Phase 3 discussed in this paper, we invested a lot of effort in improving the beam-induced background simulation for a better understanding of beam loss mechanisms in the machine. The main key improvements compared to Phase 1 and Phase 2, leading to the substantial measurement and simulation agreement, are i) the realistic collimator profile implementation in SAD, ii) particle interaction with collimator materials (tip-scattering), iii) beam-gas losses re-weighting using the measured vacuum pressure distribution around the SuperKEKB rings, iv) accurate translation of lost particle coordinates from SAD to Geant4, and v) the improved Geant4 model of the machine and detector components and the accelerator tunnel.

## 6. Extrapolations

This section estimates the expected detector background at higher luminosity based on a dedicated set of Monte-Carlo simulations. These simulations help us study machine and detector upgrades needed to achieve the planned machine performance. Below, we review our methodology for extrapolating the beam backgrounds to a luminosity of  $2.8 \times 10^{35} \text{ cm}^{-2} \text{ s}^{-1}$ , which is expected to be achieved by January 2027, before the start of LS2.

To collect an integrated luminosity of  $50 \text{ ab}^{-1}$  by the 2030s, our target instantaneous luminosity at  $\beta_y^* = 0.3 \text{ mm}$  is  $6 \times 10^{35} \text{ cm}^{-2} \text{ s}^{-1}$ . Table 8 lists predicted future beam parameters based on the most recent SuperKEKB plan for ramping up the machine [71]. Unfortunately, with the machine lattice considered in the original machine design without the Crab-Waist scheme [4], the target beam currents will be difficult or even impossible to reach because of the short beam lifetime ( $< 10 \text{ min}$ ) due to the narrow dynamic aperture [72]. Moreover, our preliminary estimates show that it may be challenging to safely run the experiment at the target beam parameters due to the low TMCI bunch current threshold for narrow collimator apertures. Thus, we might be forced to open some collimators, which could increase the IR background above the detector limits. In Ref. [14], we have proposed a few possible solutions to partially cure beam instabilities and resolve the specific luminosity and dynamic aperture degradation, where the latter affects beam lifetime, as mentioned above. Nevertheless, the upshot is that the target machine lattice and beam parameters are still too uncertain to make an accurate background prediction for the target luminosity. Therefore here, we focus on estimating backgrounds for intermediate beam parameters, which are feasible to achieve before LS2. In our simulations, the Crab-Waist

Table 8: Predicted SuperKEKB parameters, expected to be achieved by the specified date.  $\beta^*$ ,  $\mathcal{L}$ ,  $I$ ,  $BD_{\text{int.}}$ ,  $n_b$ ,  $\varepsilon$ ,  $\sigma_z$  and  $CW$  stand for the betatron function at the IP, luminosity, beam current, integrated beam dose, number of bunches, equilibrium beam emittance, bunch length and Crab-Waist sextupoles, respectively.

Setup	Before LS2	Target
Date	Jan 2027	Jan 2031
$\beta_y^*(\text{LER/HER}) [\text{mm}]$	0.6/0.6	0.27/0.3
$\beta_x^*(\text{LER/HER}) [\text{mm}]$	60/60	32/25
$\mathcal{L} [\times 10^{35} \text{ cm}^{-2} \text{ s}^{-1}]$	2.8	6.0
$I(\text{LER/HER}) [\text{A}]$	2.52/1.82	2.80/2.00
$BD_{\text{int.}} [\text{kAh}]$	45	93
$n_b [\text{bunches}]$	1576	1761
$\varepsilon_x(\text{LER/HER}) [\text{nm}]$	4.6/4.5	3.3/4.6
$\varepsilon_y/\varepsilon_x(\text{LER/HER}) [\%]$	1/1	0.27/0.28
$\sigma_z(\text{LER/HER}) [\text{mm}]$	8.27/7.60	8.25/7.58
$CW$	OFF	OFF

scheme is not used, resulting in conservative background estimates. According to preliminary, separate SAD-only simulations, the Crab-Waist scheme at  $\beta_y^* = 0.6 \text{ mm}$ , is expected to lower Belle II beam backgrounds by at least a factor of three, if simulation-optimized collimator settings can be achieved experimentally.

To project the beam-gas background forward in time, we start by extrapolating the beam pipe pressure measurements performed in 2021. Next the collimator system configuration is optimized in simulation to reduce single-beam backgrounds in the IR while maintaining an acceptable beam lifetime. Finally, we estimate all simulated background components in each sub-detector, which are then scaled by corresponding Data/MC ratios discussed above to estimate the expected background level. This results in limits on beam pipe vacuum pressure, injection quality, and collimation, which must be achieved to keep the background in Belle II sub-detectors below their rate limits.

### 6.1. Gas pressure

For the extrapolation of the residual gas pressure in each ring, we use the pressure measured by the CCGs to estimate the dynamic pressure evolution. The data were collected throughout the commissioning of SuperKEKB from 2016 until mid-2021. Figure 16 shows the estimated average  $(d\bar{P}/dI)$ , ring pressure increase per unit current at the center of the beam pipe, versus integrated beam dose ( $BD_{\text{int.}}$ ). Each calendar year of operation is emphasized with a different color and hatching style. To estimate the dynamic pressure at the beam parameters before LS2 at a luminosity of  $2.8 \times 10^{35} \text{ cm}^{-2} \text{ s}^{-1}$ , we fit only the Phase 3

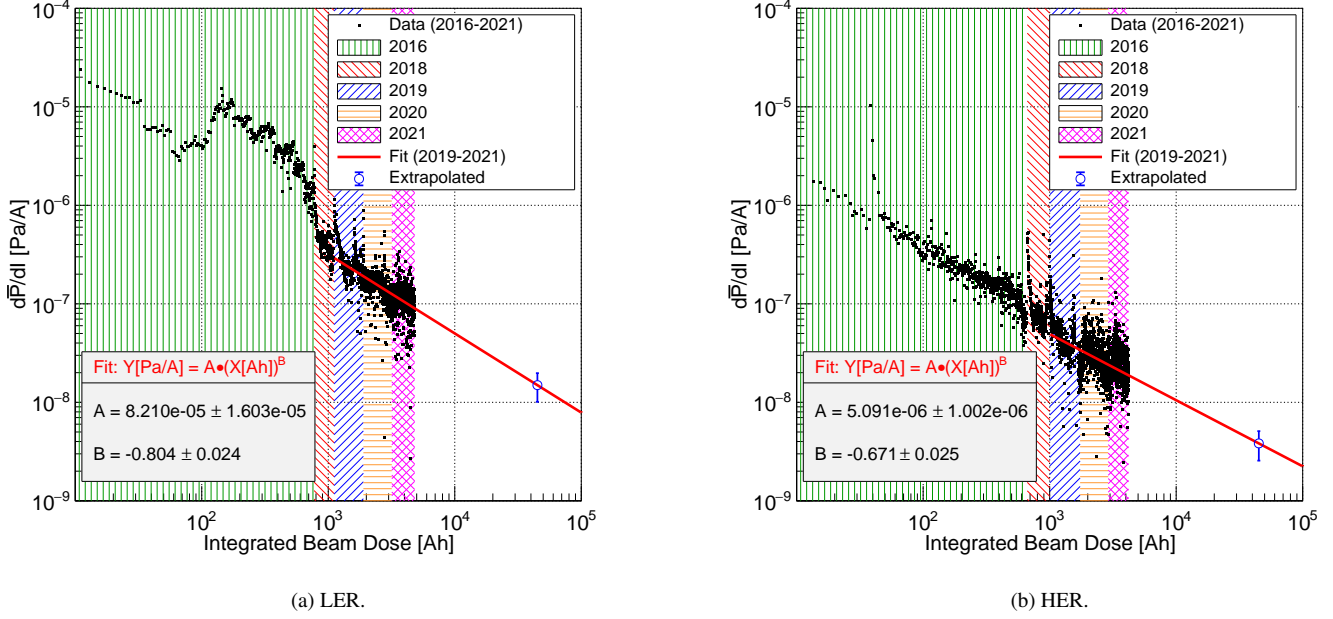


Figure 16: Beam pipe pressure increase per unit current,  $d\bar{P}/dI = 3(\bar{P}_{CCG} - \bar{P}_{0,CCG})$ , versus integrated beam dose for (a) the LER and (b) the HER. We assume  $\bar{P}_{0,CCG} = 10$  nPa. Measurements are shown as black squares.

(2019–2021) data. We assume that  $BD_{int.} = 45 \text{ kAh}^5$  will be reached by 2027 at beam currents of 2.52 A and 1.82 A for the LER and HER, respectively (Table 8). Blue, open circles in Fig. 16 show the extrapolated pressure increase per unit current for  $BD_{int.} = 45 \text{ kAh}$ . LS2 is currently planned for 2027, but there is significant uncertainty, and it may take longer to reach the integrated beam dose of 45 kAh assumed in the pressure extrapolation.

The pressure spikes seen at the beginning of each year are due to compromising the vacuum in short ring sections as part of machine maintenance work performed during standard machine shutdown periods. However, dedicated vacuum scrubbing runs, immediately after each intervention, reduce the pressure down to the nominal level. In the early stages of SuperKEKB commissioning in 2016, beam size blow-up and a non-linear residual gas pressure rise with beam current were observed in the LER [73, 74]. The growth of the positron beam emittance was caused by a fast head-tail instability, which was induced by the electron cloud effect. In 2018, this effect was cured by attaching permanent magnets and solenoids to most of the beam pipes at drift spaces in the LER. Therefore, a steep change in  $d\bar{P}/dI$  is seen between 2016 and 2018 in Fig. 16.

Assuming the base pressure for both rings is at the level of  $\bar{P}_0 = 10$  nPa, we can calculate the expected value of the beam pipe gas pressure as  $\bar{P}_{eff.} = \bar{P}_0 + d\bar{P}/dI \times I$ . Table 9 lists all results of the gas pressure extrapolation, which are then used to normalize the beam-gas background simulation.

<sup>5</sup>Rough estimate made in June 2020, which assumes that the beam is always stored at the maximum beam current ( $\sqrt{I_{LER} I_{HER}}$ ) during operation, excluding some start-up days in each run period.

Table 9: Expected beam pipe gas pressure at the beam parameters before LS2 at  $\mathcal{L} = 2.8 \times 10^{35} \text{ cm}^{-2} \text{ s}^{-1}$ , where  $d\bar{P}/dI$ ,  $\bar{P}_0$  and  $\bar{P}_{eff.}$  stand for the ring average pressure increase per unit current, base pressure and beam pipe pressure, respectively.

Term	LER	HER
$d\bar{P}/dI$ [nPa/A]	$14.94 \pm 4.83$	$3.83 \pm 1.27$
$\bar{P}_0$ [nPa]	10	10
$\bar{P}_{eff.}$ [nPa]	$47.66 \pm 12.17$	$16.97 \pm 2.31$

To simulate the expected beam-gas background at  $\mathcal{L} = 2.8 \times 10^{35} \text{ cm}^{-2} \text{ s}^{-1}$ , we use the measured gas pressure distribution along each ring from June 2021, shown in Fig. 6, and scale it to the expected vacuum pressure as follows

$$P_{CCG,i}^{est.} = P_{CCG,i}^{meas.} \times \frac{3\bar{P}_0 + d\bar{P}/dI \times I}{3\bar{P}_{CCG}^{meas.}}, \quad (16)$$

where  $P_{CCG,i}^{est.}$  and  $P_{CCG,i}^{meas.}$  are the estimated and measured gas pressure at the  $i$ -th CCG;  $\bar{P}_0$ ,  $d\bar{P}/dI$  and  $I$  are taken from Table 9;  $\bar{P}_{CCG}^{meas.}$  is the average ring pressure measured by CCGs; the factor 3 is used to take into account the vacuum conductance between the beam pipe and CCGs, see Section 4.1.1.

## 6.2. Collimation system settings

For future beam optics and beam parameters, the collimation system must be re-optimized in order to effectively protect the detector from stray beam particles. The optimization procedure [19, 23] is based on finding a compromise between very

tight collimator apertures, which reduce the beam lifetime and induce beam instabilities, and wide apertures, which increase the beam backgrounds in the IR. One of the instabilities limiting aperture tightening is TMCI, which is a wake-field effect from bunched charges traveling through the machine aperture, causing a strong head-tail instability and beam size increase. We adjust the apertures of all currently installed collimators, see Fig. 3, to satisfy the requirements listed below while maintaining the lowest possible IR backgrounds and beam lifetimes of the order of 15 minutes for both rings.

*TMCI limits relaxation.* To satisfy TMCI limits in the LER, we fully open the collimator D03V1 and set D06V2 at the aperture of the IR.

*Far distant high beam losses.* We perform primary collimation as far as possible from the IR, to reduce secondary showers reaching the detector and to protect the QCS against an abnormally injected beam. Thus we use D06V1 and D02H1 in the LER, and D09V1/3 and D12H1/2 in the HER.

*Background reduction around the IR.* Since tip-scattered particles from the collimators closest to the IP may contribute to the IR background, we shadow these collimators by tightening other upstream collimators, thereby reducing beam losses around the IR. We thus set D02H2 narrower than D02H4 in the LER, and D01H3 narrower than D01H5 in the HER. This configuration should also reduce the neutron flux toward Belle II from the closest collimators.

The optimized collimators satisfy the TMCI requirement for the predicted bunch currents before LS2 at the luminosity of  $2.8 \times 10^{35} \text{ cm}^{-2} \text{ s}^{-1}$ , which are  $I_b^{\text{LER}} = 1.60 \text{ mA}$  and  $I_b^{\text{HER}} = 1.15 \text{ mA}$ . The maximum allowed bunch currents before reaching instabilities due to collimator and IR beam pipe apertures are  $I_{\text{thresh}}^{\text{LER}} = 1.76 \text{ mA}$  and  $I_{\text{thresh}}^{\text{HER}} = 1.66 \text{ mA}$  for the LER and HER, respectively.

### 6.3. Predicted Belle II backgrounds

Figure 17 shows the predicted beam background composition in Belle II at the beam parameters before LS2 at the luminosity of  $2.8 \times 10^{35} \text{ cm}^{-2} \text{ s}^{-1}$ , see Tables 8 and 9. To obtain the expected background rates, each simulated background component is scaled by corresponding Data/MC ratios shown in Fig. 15. The predictions include systematic uncertainties associated with the variation of the Data/MC ratios among detector layers, sensors or modules. The predicted background is well below the detector limits listed in Table 4, with safety factors ranging from  $\sim 2$  to  $\sim 30$ , leaving some margin for the injection background and unexpected beam losses. In addition, the usage of the Crab-Waist scheme at  $\beta_y^* = 0.6 \text{ mm}$  potentially can enlarge the margin by an additional factor of three, as discussed above.

### 6.4. Predicted neutron flux near Belle II

The neutron flux inside Belle II is currently being studied, and detailed findings will be published separately in the future.

Here, we only provide rough estimates, based on older, completed studies in the machine tunnel.

To roughly estimate the neutron fluence in the accelerator tunnel, we assume that single-beam losses at the collimators closest to the IP are well controlled by adjusting upstream collimators. Therefore, we focus on luminosity-production of neutrons only. Based on the TPC data [22], the 1-MeV neutron equivalent fluence per Snowmass year, at a luminosity of  $2.8 \times 10^{35} \text{ cm}^{-2} \text{ s}^{-1}$  is about  $5 \times 10^{10} \text{ neq/cm}^2$  and  $5 \times 10^9 \text{ neq/cm}^2$  in the BWD and FWD tunnels, respectively [22]. At the same luminosity, our simulation predicts a  $^3\text{He}$  tube count rate due to thermal neutrons of only about  $2 \times 10^4 \text{ n/(cm}^2 \text{ s)}$  and  $4 \times 10^3 \text{ n/(cm}^2 \text{ s)}$  in the BWD and FWD tunnels, respectively. The Belle II limit for the neutron fluence ranges from  $10^{12}$  to  $10^{14} \text{ neq/cm}^2$ , as discussed in Section 2. Hence our current estimates show that the expected neutron background allows safe detector operation for more than 10 years.

### 6.5. Planned background mitigation via improved shielding

During LS1, we plan to install new or improved background shielding. We plan additional neutron shielding of Belle II to suppress the flux of neutrons originating from the accelerator tunnel and from the QCS. Although below the strict detector limits, the neutrons cause the ageing of ECL photodiodes and other detector components and lead to operationally disruptive SEU events. An additional IR bellows shield made of tungsten, and modified FWD and BWD QCS head plates, currently made of tungsten and planned to be replaced by stainless steel, are under construction and may be installed with the new pixel detector during LS1. This should reduce single-beam and luminosity backgrounds by up to 50% [75]. A new IP beam pipe with an additional gold layer and slightly modified geometry to reduce the amount of the back-scattered SR is also in production.

### 6.6. Background beyond LS2

While the Belle II backgrounds are under control, and their evolution at higher luminosity looks promising, there are other difficulties related to achieving stable machine operation while keeping acceptable background levels. In Ref. [14], we review ongoing activities and options for further background mitigation, and background predictions for even higher luminosities, up to  $6.3 \times 10^{35} \text{ cm}^{-2} \text{ s}^{-1}$ .

## 7. Conclusions

We have reported on the current beam-induced background levels in Belle II, demonstrated the accuracy of our background predictions, and estimated backgrounds for future SuperKEKB beam parameters. The beam loss simulation software, based on SAD and Geant4, has been significantly improved compared to the versions used in earlier commissioning phases, and now accurately describes the measured detector backgrounds, with Data/MC ratios within one order of magnitude of unity.



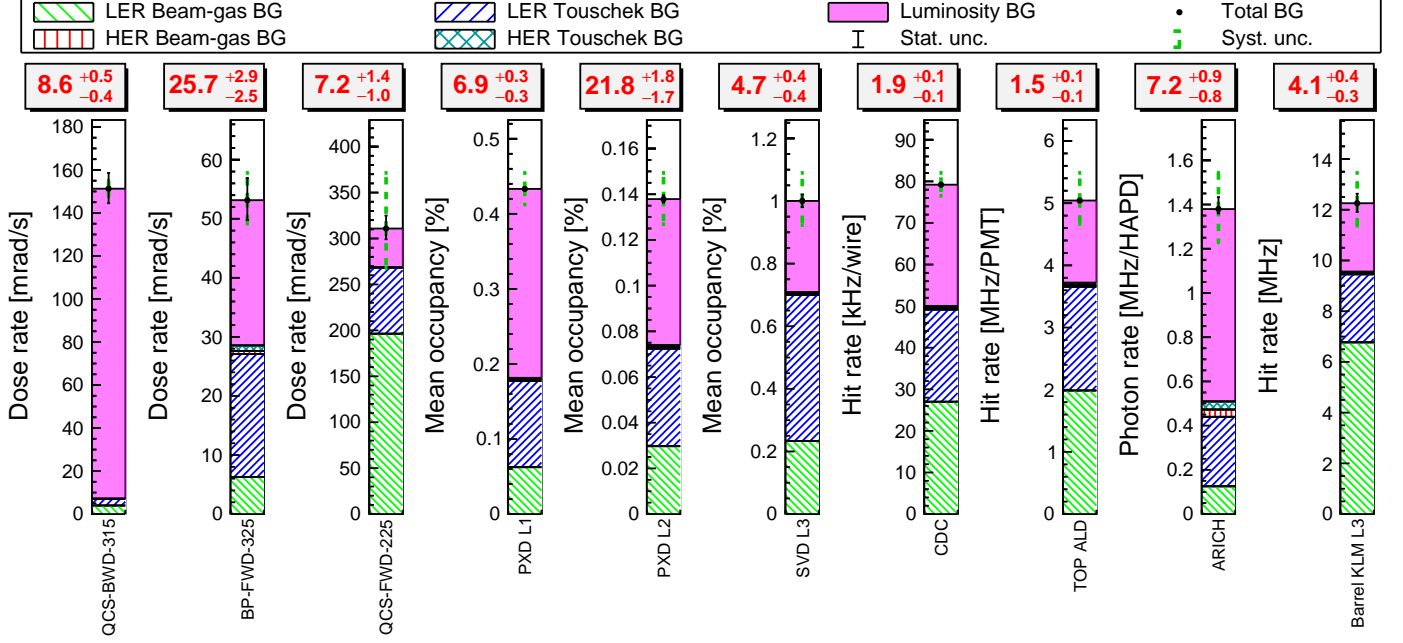


Figure 17: Estimated Belle II background composition for predicted beam parameters before LS2. Each column is a stacked histogram. The red numbers in rectangles are detector safety factors, showing that Belle II should be able to operate safely until a luminosity of  $2.8 \times 10^{35} \text{ cm}^{-2} \text{ s}^{-1}$ , with some important caveats, discussed in the text.

We want to stress that it is crucial to understand all main sources of beam losses affecting machine and detector components' longevity and causing detector performance degradation. Therefore, the accurate background prediction at the current stage is essential to trust any extrapolations, including simulation-based studies of potential SuperKEKB or Belle II upgrades. We correct the simulation for any remaining discrepancy with measurements by using the Data/MC ratios for re-scaling the simulation. But as opposed to what we had in the past at Phase 1 (2016) and Phase 2 (2018), these correction factors are now much closer to the unity, significantly increasing confidence in our methodology and extrapolations.

In early Phase 3, backgrounds from collisions of two beams at the IP, which are expected to dominate at higher luminosities, are slightly ( $\sim 20\%$ ) lower than expected. Backgrounds from single beams, which currently dominate, are a factor of four different from expectations, which is in line with the size of typical machine systematics involved, such as the beam pipe gas composition, unknown machine errors, beam instabilities, beam-beam effects, and modeling accuracy of machine components and detector surroundings.

At the current and future stages of the experiment, the most vulnerable sub-detectors are TOP and CDC, whose PMT lifetime and charged tracks reconstruction performances are strongly affected by high beam losses in the IR, respectively. Their safety factors are estimated to be at the level of  $\sim 2$  for a luminosity of  $2.8 \times 10^{35} \text{ cm}^{-2} \text{ s}^{-1}$ , leaving some margin for unpredicted or imperfectly controlled beam losses.

Currently, the most dangerous backgrounds are due to Touschek and beam-gas scattering in the LER. However, we expect that a further increase of the collision rate above  $1 \times$

$10^{35} \text{ cm}^{-2} \text{ s}^{-1}$  will raise the luminosity background to the same level as single-beam backgrounds. Based on our measurements and current understanding of beam loss mechanisms in SuperKEKB, we predict that as beam currents are increased and the beam size is decreased in the next decade, beam-induced backgrounds in Belle II will remain acceptable until at least  $\mathcal{L} = 2.8 \times 10^{35} \text{ cm}^{-2} \text{ s}^{-1}$  at  $\beta_y^* = 0.6 \text{ mm}$ . This statement assumes the baseline plan of replacing the short-lifetime conventional and ALD MCP-PMTs in the TOP detector, stable and well-controlled main ring and injection chain operation, continuous progress on vacuum scrubbing, and low impact from beam instabilities. Installing additional shielding during the two long shutdowns in 2022–2023 and around 2027 could reduce backgrounds further.

There are several important uncertainties in our projections of future backgrounds, such as unexpected and uncontrolled catastrophic beam losses, unknown sources of machine impedance, vacuum pressure at high beam doses, and possible IR beam pipe upgrades. These issues could affect our background forecast in either direction and require further studies and refinement.

Backgrounds from neutrons have been studied with dedicated detectors in the SuperKEKB tunnel. While the flux appears understood and manageable in the short term, a quantitative study that connects neutron rates to Belle II hit and SEU rates is needed, ongoing, and will be published separately in the future. SEUs deserve special scrutiny as they can reduce the operational efficiency of the experiment.

Backgrounds from injection also appear manageable but have not been projected forward, as they are not simulated from first principles. This is a challenging task that should also be

tackled in the future. Machine learning techniques appear useful in identifying the injection background, could be helpful in online machine diagnostics and may detect the most crucial parameters to be adjusted for background mitigation and collider performance improvement.

Mainly due to the uncertainties related to the design machine lattice and beam instabilities, it is too early to make accurate predictions for the distant future, but backgrounds could exceed detector limits at  $\mathcal{L} = 6 \times 10^{35} \text{ cm}^{-2} \text{ s}^{-1}$  for  $\beta_y^* = 0.3 \text{ mm}$ . Thus, several machine operation schemes, instability and background countermeasures, and upgrades of the experiment are under consideration in order to collect an integrated luminosity of the order of  $50 \text{ ab}^{-1}$  by the 2030s. We are closely collaborating with EU, US and Asian accelerator laboratories on optimizing upgrades of SuperKEKB and reaching the target luminosity.

## Acknowledgements

We thank the SuperKEKB accelerator and optics groups for the excellent machine operation and for sharing their lattice files; the KEK cryogenics group for the efficient operation of the solenoid; the KEK computing team for on-site support; our Belle II colleagues for the detector operation; G. Casarosa (INFN Pisa), D. E. Jaffe (BNL), K. Oide (CERN), B. Spruck (JGU Mainz), K. Trabelsi (IJCLab), Y. Funakoshi, N. Iida, T. Koga, H. Koiso, G. Mitsuka, K. R. Nakamura, Y. Ohnishi, Y. Suetsugu and D. Zhou (KEK) for their ideas, assistance, comments on the paper and constructive discussions. This work was supported by the U.S. Department of Energy (DOE) via Award Numbers DE-SC0010504, DE-SC0010007, and DE-SC0019230 and via U.S. Belle II Operations administered by Brookhaven National Laboratory (DE-SC0012704); the National Institute of Informatics, and Science Information NETwork 5 (SINET5), and the Ministry of Education, Culture, Sports, Science, and Technology (MEXT) of Japan. This project has received funding from the European Union's Horizon 2020 Research and Innovation programme under Grant Agreement (GA) No. 654168 and GA No. 101004761. We acknowledge the support of Grant CIDEAGENT/2018/020 of Generalitat Valenciana (Spain).

## References

- [1] T. Abe *et al.*, *Belle II Technical Design Report*, Tech. rep., KEK REPORT 2010-1 (2010). [arXiv:1011.0352](https://arxiv.org/abs/1011.0352).  
URL <https://cds.cern.ch/record/1304162>
- [2] I. Adachi, T. Browder, P. Križan, S. Tanaka, Y. Ushiroda, *Detectors for extreme luminosity: Belle II*, Nucl. Instrum. Methods Phys. Res., Sect. A 907 (2018) 46–59. [doi:10.1016/j.nima.2018.03.068](https://doi.org/10.1016/j.nima.2018.03.068).  
URL <https://www.sciencedirect.com/science/article/pii/S0168900218304200>
- [3] E. Kou *et al.*, *The Belle II Physics Book*, Prog. Theor. Exp. Phys. 2019 (12), 123C01. [doi:10.1093/ptep/ptz106](https://doi.org/10.1093/ptep/ptz106).  
URL <https://doi.org/10.1093/ptep/ptz106>
- [4] Y. Ohnishi *et al.*, *Accelerator design at SuperKEKB*, Prog. Theor. Exp. Phys. 2013 (3), 03A011. [doi:10.1093/ptep/pts083](https://doi.org/10.1093/ptep/pts083).  
URL <https://doi.org/10.1093/ptep/pts083>
- [5] N. Toge, *KEK B-factory Design Report*, Tech. rep., KEK, Tsukuba, KEK-Report-95-7 (1995).  
URL <https://cds.cern.ch/record/475260>
- [6] S. Kurokawa, E. Kikutani, *Overview of the KEKB accelerators*, Nucl. Instrum. Methods Phys. Res., Sect. A 499 (1) (2003) 1–7. [doi:10.1016/S0168-9002\(02\)01771-0](https://doi.org/10.1016/S0168-9002(02)01771-0).  
URL <https://www.sciencedirect.com/science/article/pii/S0168900202017710>
- [7] T. Abe *et al.*, *Achievements of KEKB*, Prog. Theor. Exp. Phys. 2013 (3), 03A001. [doi:10.1093/ptep/pts102](https://doi.org/10.1093/ptep/pts102).  
URL <https://doi.org/10.1093/ptep/pts102>
- [8] M. Baszczyk *et al.*, *SuperB Technical Design Report*, Tech. rep., INFN-13-01-PI, LAL-13-01, SLAC-R-1003, INFN-13-01-PI, LAL 13-01, SLAC-R-1003 (2013). [arXiv:1306.5655](https://arxiv.org/abs/1306.5655).  
URL <https://cds.cern.ch/record/1557673>
- [9] H. Nakayama, Y. Funakoshi, T. Ishibashi, K. Kanazawa, Y. Ohnishi, *SuperKEKB Background Simulations, Including Issues for Detector Shielding*, in: Proc. 55th ICFA Advanced Beam Dynamics Workshop on High Luminosity Circular e+e- Colliders – Higgs Factory (HF2014), 2015, p. 110, FRT3A1.  
URL <https://accelconf.web.cern.ch/HF2014/papers/frt3a1.pdf>
- [10] P. M. Lewis *et al.*, *First measurements of beam backgrounds at SuperKEKB*, Nucl. Instrum. Methods Phys. Res., Sect. A 914 (2019) 69–144. [doi:10.1016/j.nima.2018.05.071](https://doi.org/10.1016/j.nima.2018.05.071).  
URL <https://www.sciencedirect.com/science/article/pii/S0168900218306909>
- [11] Z. J. Liptak *et al.*, *Measurements of beam backgrounds in SuperKEKB Phase 2*, Nucl. Instrum. Methods Phys. Res., Sect. A 1040 (2022) 167168. [doi:10.1016/j.nima.2022.167168](https://doi.org/10.1016/j.nima.2022.167168).  
URL <https://www.sciencedirect.com/science/article/pii/S0168900222005149>
- [12] *Luminosity projection*, Accessed: 2022-11-27 (2022).  
URL [https://www-superkekb.kek.jp/Luminosity\\_projection.html](https://www-superkekb.kek.jp/Luminosity_projection.html)
- [13] P. Raimondi, D. Shatilov, M. Zobov, *Beam-Beam Issues for Colliding Schemes with Large Piwinski Angle and Crabbed Waist* (Jan. 2007). [doi:10.15161/oar.it/1449009600.96](https://doi.org/10.15161/oar.it/1449009600.96).  
URL <https://doi.org/10.15161/oar.it/1449009600.96>
- [14] A. Natochii *et al.*, *Beam background expectations for Belle II at SuperKEKB*, in: 2022 Snowmass Summer Study, 2022. [arXiv:2203.05731](https://arxiv.org/abs/2203.05731), [doi:10.48550/arXiv.2203.05731](https://doi.org/10.48550/arXiv.2203.05731).  
URL <https://arxiv.org/abs/2203.05731>
- [15] A. Abashian *et al.*, *The Belle detector*, Nucl. Instrum. Methods Phys. Res., Sect. A 479 (1) (2002) 117–232. [doi:10.1016/S0168-9002\(01\)02013-7](https://doi.org/10.1016/S0168-9002(01)02013-7).  
URL <https://www.sciencedirect.com/science/article/pii/S0168900201020137>
- [16] J. Brodzicka *et al.*, *Physics achievements from the Belle experiment*, Prog. Theor. Exp. Phys. 2012 (1), 04D001. [doi:10.1093/ptep/pts072](https://doi.org/10.1093/ptep/pts072).  
URL <https://doi.org/10.1093/ptep/pts072>
- [17] F. Forti, *Snowmass Whitepaper: The Belle II Detector Upgrade Program*, in: 2022 Snowmass Summer Study, 2022. [arXiv:2203.11349](https://arxiv.org/abs/2203.11349), [doi:10.48550/ARXIV.2203.11349](https://doi.org/10.48550/ARXIV.2203.11349).  
URL <https://arxiv.org/abs/2203.11349>
- [18] A. Piwinski, *The Touschek Effect in Strong Focusing Storage Rings* (1999). [doi:10.48550/ARXIV.9903034](https://doi.org/10.48550/ARXIV.9903034).  
URL <https://arxiv.org/abs/physics/9903034>
- [19] H. Nakayama, Y. Suetsugu, K. Kanazawa, Y. Ohnishi, Y. Funakoshi, K. Ohmi, D. Zou, *Small-beta collimation at SuperKEKB to stop beam-gas scattered particles and to avoid transverse mode coupling instability*, in: Proc. 3rd International Particle Accelerator Conference (IPAC2012), 2012, p. 1104, TU0BC02.  
URL <https://accelconf.web.cern.ch/IPAC2012/papers/tu0bc02.pdf>
- [20] N. Ohuchi *et al.*, *SuperKEKB beam final focus superconducting magnet system*, Nucl. Instrum. Methods Phys. Res., Sect. A 1021 (2022) 165930. [doi:https://doi.org/10.1016/j.nima.2021.165930](https://doi.org/10.1016/j.nima.2021.165930).  
URL <https://www.sciencedirect.com/science/article/pii/S0168900221008949>
- [21] B. L. Berman, S. C. Fultz, *Measurements of the giant dipole resonance with monoenergetic photons*, Rev. Mod. Phys. 47 (1975) 713–761. [doi:10.1103/RevModPhys.47.713](https://doi.org/10.1103/RevModPhys.47.713).

- URL <https://link.aps.org/doi/10.1103/RevModPhys.47.713>
- [22] J. Schueler, S. Vahsen, P. Lewis, M. Hedges, D. Liventsev, F. Meier, H. Nakayama, A. Natochii, T. Thorpe, **Application of recoil-imaging time projection chambers to directional neutron background measurements in the SuperKEKB accelerator tunnel**, Nucl. Instrum. Methods Phys. Res., Sect. A 1040 (2022) 167291. doi:10.1016/j.nima.2022.167291. URL <https://www.sciencedirect.com/science/article/pii/S0168900222006179>
- [23] A. Natochii, S. E. Vahsen, H. Nakayama, T. Ishibashi, S. Terui, **Improved simulation of beam backgrounds and collimation at SuperKEKB**, Phys. Rev. Accel. Beams 24 (2021) 081001. doi:10.1103/PhysRevAccelBeams.24.081001. URL <https://link.aps.org/doi/10.1103/PhysRevAccelBeams.24.081001>
- [24] T. Ishibashi, S. Terui, Y. Suetsugu, K. Watanabe, M. Shirai, **Movable collimator system for SuperKEKB**, Phys. Rev. Accel. Beams 23 (12) (2020) 053501. doi:10.1103/PhysRevAccelBeams.23.053501. URL <https://link.aps.org/doi/10.1103/PhysRevAccelBeams.23.053501>
- [25] A. W. Chao and M. Tigner, **Handbook of accelerator physics and engineering**, World Scientific, 1999.
- [26] Y. Ohnishi, S. Tanaka, T. Tsuboyama, M. Iwasaki, K. Kanazawa, H. Nakayama, H. Nakano, **Beam Background and MDI Design for SuperKEKB/Belle-II**, in: Proc. 2nd International Particle Accelerator Conference (IPAC2011), 2011, p. 3702, THP2010. URL <https://accelconf.web.cern.ch/IPAC2011/papers/THP2010.pdf?n=IPAC2011/papers/THP2010.pdf>
- [27] E. Mulyani, J. W. Flanagan, M. Tobiyama, H. Fukuma, H. Ikeda, G. Mitsuka, **First measurements of the vertical beam size with an X-ray beam size monitor in SuperKEKB rings**, Nucl. Instrum. Methods Phys. Res., Sect. A 919 (2019) 1–15. doi:10.1016/j.nima.2018.11.116. URL <https://www.sciencedirect.com/science/article/pii/S0168900218317686>
- [28] G. Mitsuka, KEK (private communication) (2022).
- [29] E. Kovalenko, **On-line luminosity measurements at Belle II**, J. Instrum. 15 (06) (2020) C06067. doi:10.1088/1748-0221/15/06/C06067. URL <https://dx.doi.org/10.1088/1748-0221/15/06/C06067>
- [30] Y. Suetsugu, K. Shibata, M. Shirai, **Design study of distributed pumping system using multilayer NEG strips for particle accelerators**, Nucl. Instrum. Methods Phys. Res., Sect. A 597 (2) (2008) 153–159. doi:10.1016/j.nima.2008.09.023. URL <https://www.sciencedirect.com/science/article/pii/S0168900208014058>
- [31] Y. Suetsugu, K. Shibata, T. Ishibashi, M. Shirai, S. Terui, K. Kanazawa, H. Hisamatsu, M. L. Yao, **SuperKEKB vacuum system operation in the last 6 years operation**, Phys. Rev. Accel. Beams 26 (2023) 013201. doi:10.1103/PhysRevAccelBeams.26.013201. URL <https://link.aps.org/doi/10.1103/PhysRevAccelBeams.26.013201>
- [32] S. K. Sahu, **A Generator for study of background due to beam gas interaction at KEK B-factory**, in: Proc. 2nd Workshop on Backgrounds at Machine Detector Interface, 1997, pp. 106–136, KEK-REPORT-97-10, UH-511-877-97. URL <https://lib-extopc.kek.jp/preprints/PDF/1997/9724/9724010.pdf>
- [33] S. Bacher *et al.*, **Performance of the diamond-based beam-loss monitor system of Belle II**, Nucl. Instrum. Methods Phys. Res., Sect. A 997 (2021) 165157. doi:10.1016/j.nima.2021.165157. URL <https://www.sciencedirect.com/science/article/pii/S0168900221001418>
- [34] M. Gabriel *et al.*, **A time resolved study of injection backgrounds during the first commissioning phase of SuperKEKB**, Eur. Phys. J. C 81 (11) (2021) 972. doi:10.1140/epjc/s10052-021-09769-3. URL <https://doi.org/10.1140/epjc/s10052-021-09769-3>
- [35] I. Jaegle *et al.*, **Compact, directional neutron detectors capable of high-resolution nuclear recoil imaging**, Nucl. Instrum. Methods Phys. Res., Sect. A 945 (2019) 162296. arXiv:1901.06657, doi:10.1016/j.nima.2019.06.037.
- [36] S. R. de Jong, **Study of Thermal Neutron Flux from SuperKEKB in the Belle II Commissioning Detector**, Ph.D. thesis, University of Victoria, Victoria BC, BELLE2-PHESIS-2018-002 (2017). URL <https://docs.belle2.org/record/1066>
- [37] H. Ikeda, M. Arinaga, J. W. Flanagan, H. Fukuma and M. Tobiyama, **Beam loss monitor at SuperKEKB**, in: Proc. International Beam Instrumentation Conference (IBIC'14), 2014, pp. 459–462, TUPD22. URL <https://accelconf.web.cern.ch/ibic2014/papers/tupd22.pdf>
- [38] H. Schreeck, B. Paschen, P. Wieduwilt, P. Ahlburg, L. Andricek, J. Dingfelder, A. Frey, F. Lütticke, C. Marinas, R. Richter, B. Schwenker, **Effects of gamma irradiation on DEPFET pixel sensors for the Belle II experiment**, Nucl. Instrum. Methods Phys. Res., Sect. A 959 (2020) 163522. doi:10.1016/j.nima.2020.163522. URL <https://www.sciencedirect.com/science/article/pii/S0168900220301133>
- [39] G. Lindström, S. Watts, F. Lemeilleur, **3rd RD48 status report**, Tech. rep., CERN, Geneva, CERN-LHCC-2000-009 (1999). URL <https://cds.cern.ch/record/421210>
- [40] P. Casolaro, L. Campajola, D. De Luca, **Neutrons for studies of radiation hardness**, Nuovo Cim. C 43 (2-3) (2020) 57. doi:10.1393/ncc/i2020-20057-8. URL <https://www.sif.it/riviste/sif/ncc/econtents/2020/043/02-03/article/37>
- [41] B. Aubert *et al.*, **The BaBar detector: Upgrades, operation and performance**, Nucl. Instrum. Methods Phys. Res., Sect. A 729 (2013) 615–701. doi:10.1016/j.nima.2013.05.107. URL <https://www.sciencedirect.com/science/article/pii/S0168900213007183>
- [42] Y. Uematsu *et al.*, **The Silicon Vertex Detector of the Belle II experiment**, Nucl. Instrum. Methods Phys. Res., Sect. A 1033 (2022) 166688. doi:10.1016/j.nima.2022.166688. URL <https://www.sciencedirect.com/science/article/pii/S0168900222002315>
- [43] L. Massaccesi, F. Forti, **Performance study of the SVD detector of Belle II and future upgrades**, Master's thesis, Università di Pisa, Pisa, BELLE2-MTHESIS-2021-078 (2021). URL <https://docs.belle2.org/record/2759/>
- [44] T. Higuchi, M. Nakao, E. Nakano, **Radiation tolerance of readout electronics for Belle II**, J. Instrum. 7 (02) (2012) C02022. doi:10.1088/1748-0221/7/02/C02022. URL <https://dx.doi.org/10.1088/1748-0221/7/02/C02022>
- [45] V. Bertacchi *et al.*, **Track finding at Belle II**, Comput. Phys. Commun. 259 (2021) 107610. doi:10.1016/j.cpc.2020.107610. URL <https://www.sciencedirect.com/science/article/pii/S0010465520302861>
- [46] R. Giordano, Y. Lai, S. Korpar, R. Pestotnik, A. Lozar, L. Šantelj, M. Shoji, S. Nishida, **Frame-Level Intermodular Configuration Scrubbing of On-Detector FPGAs for the ARICH at Belle II**, IEEE Trans. Nucl. Sci. 68 (12) (2021) 2810–2817. doi:10.1109/TNS.2021.3127446. URL <https://ieeexplore.ieee.org/document/9611780>
- [47] K. Matsuoka, S. Hirose, T. Iijima, K. Inami, Y. Kato, K. Kobayashi, Y. Maeda, R. Omori, K. Suzuki, **Extension of the MCP-PMT lifetime**, Nucl. Instrum. Methods Phys. Res., Sect. A 876 (2017) 93–95. doi:10.1016/j.nima.2017.02.010. URL <https://www.sciencedirect.com/science/article/pii/S0168900217301912>
- [48] **Strategic Accelerator Design**, SAD Home Page, Accessed: 2022-11-27 (2022). URL <http://acc-physics.kek.jp/SAD/>
- [49] J. D. Jackson, **Classical Electrodynamics**, John Wiley & Sons, Inc., 1962.
- [50] H. Bethe and W. Heitler, **On the Stopping of fast particles and on the creation of positive electrons**, Proc. R. Soc. A: Math. Phys. Eng. Sci. 146 (1934) 83–112. doi:10.1098/rspa.1934.0140. URL <https://royalsocietypublishing.org/doi/10.1098/rspa.1934.0140>
- [51] H. W. Koch, J. W. Motz, **Bremsstrahlung Cross-Section Formulas and Related Data**, Rev. Mod. Phys. 31 (1959) 920–955. doi:10.1103/RevModPhys.31.920. URL <https://link.aps.org/doi/10.1103/RevModPhys.31.920>
- [52] Chr. Möller, **Zur Theorie des Durchgangs schneller Elektronen durch Materie**, Ann. Phys. 406 (5) (1932) 531–585. doi:10.1002/andp.19324060506. URL <https://onlinelibrary.wiley.com/doi/abs/10.1002/andp.19324060506>

- [andp.19324060506](#)
- [53] H. Bruck, *Circular particle accelerators*, 1974, LA-TR-72-10-REV, LA-TR-72-10.  
URL <https://inspirehep.net/literature/19864>
- [54] S. Agostinelli *et al.*, *Geant4 — a simulation toolkit*, Nucl. Instrum. Methods Phys. Res., Sect. A 506 (3) (2003) 250–303. doi:10.1016/S0168-9002(03)01368-8.  
URL <https://www.sciencedirect.com/science/article/pii/S0168900203013688>
- [55] J. Allison *et al.*, *Geant4 developments and applications*, IEEE Trans. Nucl. Sci. 53 (1) (2006) 270–278. doi:10.1109/TNS.2006.869826.  
URL <https://ieeexplore.ieee.org/document/1610988>
- [56] J. Allison *et al.*, *Recent developments in Geant4*, Nucl. Instrum. Methods Phys. Res., Sect. A 835 (2016) 186–225. doi:10.1016/j.nima.2016.06.125.  
URL <https://www.sciencedirect.com/science/article/pii/S0168900216306957>
- [57] T. Kuhr, C. Pulvermacher, M. Ritter, T. Hauth, N. Braun, The Belle II Core Software, Comput. Softw. Big Sci. 3 (1) (2019) 1. arXiv:1809.04299, doi:10.1007/s41781-018-0017-9.
- [58] Belle II collaboration, Belle II Analysis Software Framework (basf2), <https://doi.org/10.5281/zenodo.5574115>.
- [59] Geant4, Reference Physics Lists, [https://geant4-userdoc.web.cern.ch/UsersGuides/PhysicsListGuide/html/reference\\_PL/index.html](https://geant4-userdoc.web.cern.ch/UsersGuides/PhysicsListGuide/html/reference_PL/index.html).
- [60] R. Kleiss, H. Burkhardt, *BBBREM — Monte Carlo simulation of radiative Bhabha scattering in the very forward direction*, Comput. Phys. Commun. 81 (3) (1994) 372–380. doi:10.1016/0010-4655(94)90085-X.  
URL <https://www.sciencedirect.com/science/article/pii/001046559490085X>
- [61] S. Jadach, W. Placzek, B. Ward, *BHWIDE 1.00:  $O(\alpha)$  YFS exponentiated Monte Carlo for Bhabha scattering at wide angles for LEP1/SLC and LEP2*, Phys. Lett. B 390 (1) (1997) 298–308. doi:10.1016/S0370-2693(96)01382-2.  
URL <https://www.sciencedirect.com/science/article/pii/S0370269396013822>
- [62] F. Berends, P. Daverveldt, R. Kleiss, *Complete lowest-order calculations for four-lepton final states in electron-positron collisions*, Nucl. Phys. B 253 (1985) 441–463. doi:10.1016/0550-3213(85)90541-3.  
URL <https://www.sciencedirect.com/science/article/pii/0550321385905413>
- [63] A. Wolski, *Beam dynamics in high energy particle accelerators*, Imperial College Press, 2014.
- [64] G. Mitsuka, *Realizing High Luminosity at SuperKEKB*, in: Proc. 3rd J-PARC Symposium (J-PARC2019), Vol. 33, 2021, p. 011007. doi:10.7566/JPSCP.33.011007.  
URL <https://journals.jps.jp/doi/abs/10.7566/JPSCP.33.011007>
- [65] H. Ikeda, KEK (private communication) (2021).
- [66] B. Schwenker, L. Herzberg, Y. Buch, A. Frey, A. Natochii, S. Vahsen, H. Nakayama, *A neural network for beam background decomposition in Belle II at SuperKEKB* (2023). doi:10.48550/ARXIV.2301.06170.  
URL <https://arxiv.org/abs/2301.06170>
- [67] M. Sundararajan, A. Taly, Q. Yan, *Axiomatic Attribution for Deep Networks* (2017). doi:10.48550/ARXIV.1703.01365.  
URL <https://arxiv.org/abs/1703.01365>
- [68] G. Erion, J. D. Janizek, P. Sturmfels, S. Lundberg, S.-I. Lee, *Improving performance of deep learning models with axiomatic attribution priors and expected gradients* (2019). doi:10.48550/ARXIV.1906.10670.  
URL <https://arxiv.org/abs/1906.10670>
- [69] N. Norris, *The Standard Errors of the Geometric and Harmonic Means and Their Application to Index Numbers*, Ann Math Stat. 11 (4) (1940) 445–448. doi:10.1214/aoms/1177731830.  
URL <https://doi.org/10.1214/aoms/1177731830>
- [70] E. F. Alf, J. M. Grossberg, *The geometric mean: Confidence limits and significance tests*, Percept. Psychophys. 26 (5) (1979) 419–421. doi:10.3758/BF03204171.  
URL <https://link.springer.com/article/10.3758/BF03204171>
- [71] Y. Suetsugu, KEK (private communication) (2021).
- [72] A. Morita, *Crab Waist Scheme for SuperKEKB*, ICFA Beam Dyn. Newslett. 67 (2015) 35–40.  
URL <https://inspirehep.net/files/074ac5a9da88433f01eac3c6b3f4c03e>
- [73] K. Ohmi, J. Flanagan, H. Fukuma, H. Ikeda, E. Mulyani, K. Shibata, Y. Suetsugu, M. Tobiyama, *Electron cloud effects in SuperKEKB commissioning*, in: Proc. Joint INFN-CERN-ARIES Workshop on Electron-Cloud Effects (ELOUD’18), Vol. 7, 2020, pp. 179–182, CERN-2020-007. doi:10.23732/CYRCP-2020-007.179.  
URL <https://cds.cern.ch/record/2737329>
- [74] Y. Suetsugu, H. Fukuma, K. Ohmi, M. Tobiyama, K. Shibata, *Electron cloud effect and its cures in the SuperKEKB positron ring*, in: Proc. Joint INFN-CERN-ARIES Workshop on Electron-Cloud Effects (ELOUD’18), Vol. 7, 2020, pp. 201–208, CERN-2020-007. doi:10.23732/CYRCP-2020-007.201.  
URL <https://journals.jps.jp/doi/abs/10.7566/JPSCP.33.011007>
- [75] K. R. Nakamura, KEK (private communication) (2021).